Food and Bioproducts Processing 144 (2024) 110–122

Contents lists available at ScienceDirect

Food and Bioproducts Processing

journal homepage: www.elsevier.com/locate/fbp

A scalable biomanufacturing platform for bacterial magnetosomes☆

Alfred Fernández-Castané [a,b,c,1], Hong Li [a,1,2], Moritz Ebeler [d,3], Matthias Franzreb [d], Tim W. Overton [a,b], Owen R.T. Thomas [a,*]

[a] School of Chemical Engineering, University of Birmingham, Birmingham B15 2TT, UK
[b] Institute for Microbiology & Infection, University of Birmingham, Birmingham B15 2TT, UK
[c] Energy and Bioproducts Research Institute, Aston University, Birmingham B4 7ET, UK
[d] Institute of Functional Interfaces, Karlsruhe Institute of Technology, Germany

ARTICLE INFO

Keywords:
Aqueous two-phase systems, ATPS
Bioprocess separations
Downstream processing, DSP
Magnetic nanoparticles, MNP
Magnetotactic bacteria, MTB
Purification

ABSTRACT

An integrated scalable platform for fermentative production and downstream processing of bacterial magnetosome products is advanced. Long magnetosome chains, high cellular magnetism, and low numbers of polyhydroxyalkanoate granules were obtained during the exponential growth phase of a two-stage continuous high cell density fermentation of *M. gryphiswaldense* MSR-1. Centrifugally concentrated 20% (w/v) suspensions of exponential phase cells were disrupted with high efficiency (~92%) in a single pass through a Constant Systems Cell Disruptor operated at 10 kpsi, releasing ~75% of the cellular iron. Magnetosomes were recovered in partially purified form from crude whole cell disruptates by rotor-stator high-gradient magnetic separation. Further purification/polishing was achieved by magnetically enhanced density separation in an aqueous micellar two-phase system (a new technique developed in this work as a low-cost alternative to sucrose gradient ultracentrifugation). The unoptimised 4-step process delivered highly purified magnetosomes (ca. 50 and 80-fold with respect to polyhydroxyalkanoate and protein) in > 50% yield, with no evidence of crystal coat damage, acceptable reduction (~35%) in median magnetosome chain length, and magnetic properties (pot-bellied hysteresis loop, coercivity = 9.8 mT, 'squareness' = 0.32) expected of isolated magnetosome chains. Though demonstrated in batch mode, the platform displays potential for end-to-end continuous manufacture of future magnetosome-based products.

1. Introduction

Applications of magnetic nanoparticles (MNPs) are growing at a staggering pace, driven in large part by the myriad uses envisaged for such materials in diverse areas including but not limited to bioremediation, information and energy storage, catalysis, cellular biotechnology, food safety and especially medicine (Ali et al., 2021; Gul et al., 2019; Majidi et al., 2016).

The vast majority of MNPs are manufactured by chemical and/or physical methods (Ali et al., 2016). Common disadvantages of these methods include complexity, expense, use of extreme temperatures and/or pressures, need for stringent control of or complete elimination of oxygen, use of solvents and surfactants, low yields and poor scale-up potential, significant variation between batches, instability, and in most cases, the need to coat, modify and functionalise MNPs post synthesis (Ali et al., 2016, 2021; Majidi et al., 2016). Many of these issues could be eliminated by 'greener' biological approaches exploiting the metal uptake and biomineralization capacity of intact fungal, plant and bacterial cells (Alphandéry, 2020; Ben-Shimon et al., 2021; Gul et al., 2019; Majidi et al., 2016), or of key components isolated from them and employed in vitro (Gul et al., 2019; Majidi et al., 2016; Peigneux et al., 2016; Rawlings et al., 2019). Of these MNPs, those naturally produced by magnetotactic bacteria (MTB), of which there are great many types (Ben-Shimon et al., 2021; Blakemore, 1975; Frankel and Blakemore,

☆ The original article was received on 5 October 2023, peer reviewed and accepted in error before revisions could be done, so a revised manuscript had to be summitted on 11 January after which it was reviewed again and finally accepted.

* Corresponding author.
E-mail address: o.r.t.thomas@bham.ac.uk (O.R.T. Thomas).

[1] These authors contributed equally.
[2] Present addresses: Wuxi Biologics Co. Ltd., Wuxi 214092, China
[3] Present addresses: Boehringer Ingelheim Pharma GmbH & Co. KG, Birkendorfer Str. 65, DE-88397 Biberach an der Riß, Germany.

https://doi.org/10.1016/j.fbp.2024.01.005
Received 11 January 2024; Accepted 12 January 2024
Available online 17 January 2024

1980), exhibit characteristics that make them particularly attractive for biomedical applications; notably for detection (Boucher et al., 2017; Lee et al., 2011; Vargas et al., 2018) and hyperthermic treatment of tumours (Alphandéry et al., 2011, 2012, 2013; Plan Sangnier et al., 2018; Sun et al., 2011; Vargas et al., 2018) and, drug and gene delivery (Sun et al., 2011; Vargas et al., 2018; Wang et al., 2018). These MNPs, referred to as magnetosomes, are sub-cellular nanoscale organelles that serve as passive navigational devices, i.e., compasses (Blakemore, 1975; Frankel and Blakemore, 1980; Schüler, Frankel, 1999).

Magnetosomes comprise highly ordered chains of single-domain (SD) permanently magnetic crystals of magnetite (Fe_3O_4) or greigite (Fe_3S_4) (Bazylinski et al., 1994), each wrapped in an elaborate phospholipid membrane decorated with membrane-associated and magnetic particle membrane-specific proteins (Gorby et al., 1988; Schüler, Frankel, 1999) and tethered to an actin-like protein filament aligned with the cell's axis (Ben-Shimon et al., 2021; Scheffel et al., 2006). Owing to strong magnetostatic intrachain interactions between contiguous magnetic crystals units along the chain axis, the magnetosome chain behaves as an elongated SD particle with a moment equal to the sum of the individual particle moments within the chain (Denham et al., 1980; Frankel and Blakemore, 1980; Orue et al., 2018).

Biologically synthesised magnetosomes afford a unique combination of properties not currently matched by chemically made MNPs, i.e.: (i) their unusual magnetic character (Orue et al., 2018; Moskowitz et al., 1988) and high heating capacity (Alphandéry et al., 2011, 2012, 2013) courtesy of defined crystal morphology and narrow size distribution in the SD range, high crystal purity with few defects, and organisation of magnetosomes as chains (Bazylinski et al., 1994; Denham et al., 1980; Frankel and Blakemore, 1980; Grünberg et al., 2001; Scheffel et al., 2006; Vargas et al., 2018); (ii) resistance to aggregation and facile dispersion in aqueous media given that each crystal is encased in a stable coating (Heyen and Schüler, 2003); and (iii) ease with which the surfaces of magnetosomes can be modified in vitro post synthesis (Hamdous et al., 2017; Wacker et al., 2007) or in vivo using genetic engineering tools (Borg et al., 2015; Hafsi et al., 2020; Lang and Schüler, 2008; Mickoleit et al., 2018).

The lack of large-scale biomanufacturing knowhow remains a significant obstacle to realising future applications of magnetosome products (Berny et al., 2020; Fernández-Castané et al., 2017; 2018; 2021; Guo et al., 2011; Jacob and Suthindhiran, 2016; Rosenfeldt et al., 2021; Yang et al., 2013). While considerable research effort has focused on upstream fermentative strategies to improve magnetosome yield and quality (Berny et al., 2020; Fernández-Castané et al., 2018; Heyen and Schüler, 2003; Liu et al., 2010; Sun et al., 2008; Yang et al., 2013; Zhang et al., 2011), very little has been done on developing downstream processes for magnetosomes (Guo et al., 2011). Most lab scale isolation and purification procedures described today are little different to those described 35 years earlier by Gorby et al. (1988), and only one study details a standardised approach to magnetosome recovery and purification in the laboratory (Rosenfeldt et al., 2021). Though several authored works promise provision of highly pure magnetosomes in large quantity (Berny et al., 2020; Guo et al., 2011; Rosenfeldt et al., 2021) none of the routes reported thus far afford true potential for translation to manufacturing scales employed/expected by the biopharma sector, as key steps at the centre of all, employ inappropriate and 'difficult-to--scale' technologies, i.e., ultrasonication, permanent bar magnets, MACS columns, sucrose density gradient ultracentrifugation. While some applications permit the use of harsher procedures, i.e., those calling for single magnetosomes and/or the removal of the magnetosome membrane prior to surface modifying the magnetic crystals (Vargas et al., 2018), important others, e.g., magnetic hyperthermia, require gentle processing that preserves integrity of magnetosome chain, their membrane and specific complement of proteins (Alphandéry et al., 2011, 2012, 2013; Vargas et al., 2018). Here, we chart the development of an integrated scalable platform for magnetosome production, which replaces standard lab-scale operations with ones proven at technical or process scale for the recovery of proteins and is gentle on product.

2. Materials and methods

2.1. Strains, growth media and culture conditions

Magnetospirillum gryphiswaldense MSR-1 was obtained from Deutsche Sammlung von Mikroorganismen und Zellkulturen GmbH (DSMZ, Germany) and used for all experiments. Unless indicated otherwise, all chemicals were purchased from Sigma-Aldrich (Poole, Dorset, UK). Cryostocks of *M. gryphiswaldense* in 5% (v/v) DMSO were routinely grown in flask standard medium (FSM): 3.5 $g{\cdot}L^{-1}$ potassium l-lactate; 100 μM iron citrate; 0.1 $g{\cdot}L^{-1}$ KH_2PO_4; 0.15 $g{\cdot}L^{-1}$ $MgSO_4{\cdot}7\ H_2O$; 2.38 $g{\cdot}L^{-1}$ HEPES; 0.34 $g{\cdot}L^{-1}$ $NaNO_3$; 0.1 $g{\cdot}L^{-1}$ yeast extract; 3 $g{\cdot}L^{-1}$ soybean peptone; and 1 $mL{\cdot}L^{-1}$ EDTA-chelated trace element solution (Widdel and Bak,1992) replacing $MnCl_2$ for $MnSO_4{\cdot}H_2O$. EDTA-TES contained: 5.2 $g{\cdot}L^{-1}$ EDTA disodium salt; 2.1 $g{\cdot}L^{-1}$ $FeSO_4{\cdot}7\ H_2O$; 30 $mg{\cdot}L^{-1}$ H_3BO_3; 85.4 $mg{\cdot}L^{-1}$ $MnSO_4{\cdot}H_2O$; 190 $g{\cdot}L^{-1}$ $CoCl_2$ $g{\cdot}L^{-1}$; 4 $mg{\cdot}L^{-1}$ $NiCl_2{\cdot}6\ H_2O$; 2 $mg{\cdot}L^{-1}$ $CuCl_2{\cdot}2\ H_2O$; 44 $mg{\cdot}L^{-1}$ $ZnSO_4{\cdot}7\ H_2O$ and 36 $mg{\cdot}L^{-1}$ $Na_2MoO_4{\cdot}2\ H_2O$. Pre-cultures used for bioreactor inoculation were grown in FSM without iron citrate. The pH of FSM was adjusted to 7.0 with NaOH (Heyen and Schüler, 2003). Cells were grown at 30 °C in a shaker incubator at 150 rpm.

The batch medium for bioreactor experiments consisted of FSM without iron citrate and feed solution contained: 100 $g{\cdot}L^{-1}$ lactic acid; 3 or 25 $g{\cdot}L^{-1}$ $NaNO_3$; 18 $mL{\cdot}L^{-1}$ 25 – 28% $NH_3{\cdot}H_2O$; 6 $g{\cdot}L^{-1}$ yeast extract; 2.4 $g{\cdot}L^{-1}$ $MgSO_4{\cdot}7\ H_2O$; 6 g L^{-1} $K_2HPO_4{\cdot}3\ H_2O$; 70 $mL{\cdot}L^{-1}$ Mineral Elixir and 2 $g{\cdot}L^{-1}$ $FeCl_3{\cdot}6\ H_2O$. The mineral elixir (pH 7) contained: 1.5 $g{\cdot}L^{-1}$ nitrilotriacetic acid; 3 $g{\cdot}L^{-1}$ $MgSO_4{\cdot}7\ H_2O$; 0.5 $g{\cdot}L^{-1}$ $MnSO_4{\cdot}2\ H_2O$; 1 $g{\cdot}L^{-1}$ NaCl; 0.1 $g{\cdot}L^{-1}$ $FeSO_4{\cdot}7\ H_2O$; 0.18 $g{\cdot}L^{-1}$ $CoSO_4{\cdot}7\ H_2O$; 0.1 $g{\cdot}L^{-1}$ $CaCl_2{\cdot}2\ H_2O$; 0.18 $g{\cdot}L^{-1}$ $ZnSO_4{\cdot}7\ H_2O$; 0.01 $g{\cdot}L^{-1}$ $CuSO_4{\cdot}5\ H_2O$; 0.02 $g{\cdot}L^{-1}$ $KAl(SO_4)_2{\cdot}12\ H_2O$; 0.01 $g{\cdot}L^{-1}$ H_3BO_3; 0.01 $g{\cdot}L^{-1}$ $Na_2MoO_4{\cdot}2\ H_2O$; 0.03 $g{\cdot}L^{-1}$ $NiCl_2{\cdot}6\ H_2O$ and 0.3 $g{\cdot}L^{-1}$ $Na_2SeO_3{\cdot}5\ H_2O$.

2.2. Bioreactor set-up

Two fermentation strategies were employed in this work, i.e., a simple pH-stat fed-batch we introduced earlier (Fernández-Castané et al., 2018) employing 3 $g{\cdot}L^{-1}$ $NaNO_3$, and the two-stage continuous process described below with 25 $g{\cdot}L^{-1}$ $NaNO_3$.

An Electrolab (Tewkesbury, UK) Fermac 310/60 5-L jar bioreactor (3 L working volume) equipped with four baffles and an agitator featuring two six-bladed Rushton turbines was used. Aeration was achieved by sparging beneath the lower impeller at a rate of 0 – 100 $mL{\cdot}min^{-1}$, through a reusable, autoclavable 0.22-μm filter (Sartorius Stedim Biotech GmbH, Göttingen, Germany). Dissolved oxygen in the medium (pO_2) was measured online using a D150 Oxyprobe (Broadley-James Ltd, Bedford, Beds, UK). Agitation was maintained at 100 – 500 rpm. An F-695 FermProbe (Broadley-James Ltd, Bedford, Beds, UK) was employed to measure pH and was controlled to a set-point of 7.0 ± 0.05 by automated addition of an acidic feed solution (pH-stat mode). Upon reaching an OD_{565} of ca. 5 the broth volume was kept constant with the aid of a stainless-steel tube fitted through the headplate ending at the air-liquid interface. Excess broth was removed using a peristaltic pump, at a constant flow rate of 40 $mL{\cdot}min^{-1}$ directed to an outlet reservoir, thus resulting in a second stage of fermentation operated in continuous mode. Off-gas passed through a condenser, an autoclavable 0.22-μm filter (Sartorius Stedim Biotech GmbH, Göttingen, Germany) and a HEPA filter (Merck KGaA, Darmstadt, Germany). The temperature was maintained at 30 °C by means of a heating jacket and a cold finger (Fernández-Castané et al., 2018).

2.3. Cell harvesting and disruption

MSR-1 cells were harvested by centrifugation in a Beckman J2–21 centrifuge (7500 g_{av}, 20 min, 4 °C), and stored at − 18 °C until required.

Frozen cell pastes were thawed on ice before resuspending in 50 mM HEPES buffer, pH 8.0, to a final wet cell concentration of 20% (w/v).

Small scale disruptions were performed using 6 mL portions of cell suspension contained in 15 mL Falcon tubes. Cells were either: (i) disrupted on ice using a Status US70 ultrasonic (20 kHz, 60 W) probe sonicator (Philip Harris Scientific, Lichfield, Staffs, UK) operated in ten bursts of 1 min duration (50% duty cycle) at 70% amplitude (power) with 1 min cooling of the probe in ice cold water between bursts; or (ii) treated in an L&R Ultrasonics 55 W T-9 ultrasonic bath (L&R Manufacturing Company, Kearny, NJ, USA) for 0.5 to 2 h. High-pressure homogenization trials were initially conducted with 50 mL volumes of cell suspension using a 0.75 kW TS Bench Top High Pressure Cell Disruptor (Constant Systems Ltd, Daventry, Northants, UK) operated at various disruption pressures, *P* (5 – 20 kpsi) using 1 – 5 discrete passes, *N*. In later experiments larger quantities of cell suspension (250 mL) were subjected to a single pass at 10 kpsi.

2.4. Magnetic separations

Powerful Neodymium-Iron-Boron (NdFeB) permanent magnet blocks of various sizes (50 ×15 ×15, 60 ×30 ×15 and 110 ×89 ×19.5 mm; Supermagnete, Gottmadingen, Germany) were variously employed in this work (for small-scale magnetosome recovery, concentrating magnetosome containing process liquors, demonstrating magnetically enhanced density separation, MEDS). High-gradient magnetic separation (HGMS) was used to recover magnetosomes from large volumes of disrupted MSR-1 cells.

2.4.1. Description of the rotor-stator high-gradient magnetic separator (RS-HGMS) system

The magnetic separator model 'chemagic 15 Durchfluss-Separator Birmingham' (PerkinElmer chemagen Technologie GmbH, Baesweiler, Germany) employed in this study is based on Franzreb and Reichert's (2006) patented 'rotor-stator' magnetic filter system and is an improved version of the earlier similarly sized ProMagic system used by Brown et al. (2013).

The main components of the RS-HGMS system (Fig. 1) include: (i) an air-cooled 'ON/OFF' 0.28 T solenoid electromagnet equipped with bore temperature measurement; (ii) a separator chamber within the magnet bore housing a specially designed 'rotor-stator' magnetic filter arrangement coupled to a variable speed motor; (iii) a hollow copper coil between the separator chamber and the magnet bore for 'active cooling' with chilled (4 °C) tap water; (iv) a variable speed bidirectional peristaltic pump; (v) two computer-controlled six-way valves for regulating liquid flow within the RS-HGMS rig (Fig. 1a); (vi) a laptop computer equipped with TwinCAT IO control software (Beckhoff Automation GmbH & Co KG, Verl, Germany) and Altova Authentic® protocol editing software (Altova GmbH, Vienna, Austria); and (vii) Duran bottles of various size used as reservoirs for feedstock, wash/elution buffer and CIP solution and for collecting fractions. The 'rotor-stator' filter (internal diameter = 60 mm; working volume = 250 mL) features a rotating shaft mounted with densely perforated discs interlocked with a two-part stationary assembly of densely perforated discs, to create an alternating arrangement of rotatable and fixed filter disks, spaced 3 mm apart (Fig. 1c & d) which play the role of matrix wires employed in conventional HGMS systems. Once programmed, the laptop computer was able to record the temperature of the magnet, and control: the switching of the valve positions; the speed and direction of the pump; rotation of the rotor; and switching the magnet ON and OFF as required.

2.4.2. Recovery of magnetosomes from disrupted M. gryphiswaldense MSR-1 cells by RS-HGMS

Prior to commencing RS-HGMS, ice cold (4 °C) 50 mM HEPES buffer pH 8.0 was recirculated through the whole system for 5 min at 14.4 L·h^{-1} at 'zero field' with the stirrer OFF. Following system equilibration, 250 mL of cell disruptate (prepared by single pass disruption of a 20% (w/v) suspension of exponential phase *M. gryphiswaldense* MSR-1 in 50 mM HEPES buffer pH 8.0 at 10 kpsi) was applied to the filter at a flow rate of either 0.6 or 3.6 L·h^{-1} with the magnetic field turned ON and stirrer OFF. Magnetosomes were captured in the magnetized filter, whereas magnetosome-depleted feedstock passed through and was collected as the 'flowthrough' fraction. Subsequently, with the field ON, 250 mL of 50 mM HEPES buffer, pH 8.0, was pumped through the filter at either 0.6 L·h^{-1} or 3.6 L·h^{-1} to flush out residually entrained feedstock material and fill the filter and lines with the wash buffer. The output from the rig was collected, before stopping the pump and resuspending the magnetosome particles in wash buffer by switching the magnetic field OFF and the stirrer ON for 1 min at 600 rpm (50% rotor power). Recollection of magnetosomes was initiated by switching the stirrer OFF and the magnetic field back ON for 1 min (without pumping the process stream around the recycle loop), before initiating the next

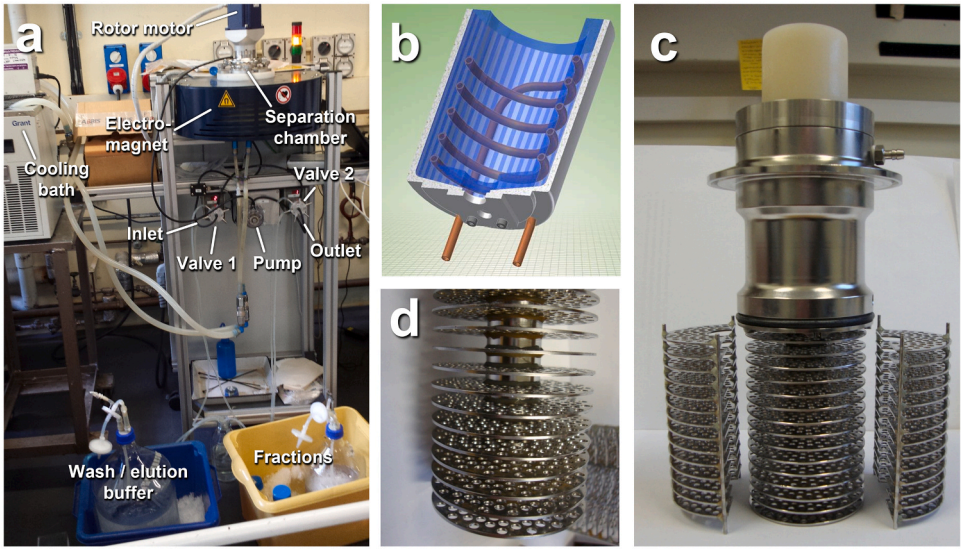

Fig. 1. (a) Annotated photograph of the chemagic 15 RS-HGMS set-up employed in this work. **(b)** Schematic of the filter chamber's active cooling system (the coil winding density is greater than illustrated). **(c)** Disassembled filter showing perforated filter discs mounted on a rotating shaft and two-part stationary perforated filter assembly. **(d)** Close-up of rotating filter discs showing the perforations.

cycle by continuing collection of the washings at a flow rate of 0.6 or 3.6 $L{\cdot}h^{-1}$ for 2 min. This washing regime was carried out three times, and the washes from the cycles were collected separately. Subsequently, the first of several sequential elution cycles was performed by pumping wash buffer into the filter at 7.2 $L{\cdot}h^{-1}$ at 'zero field' without stirring. The flow was then stopped, and the stirrer switched ON for 2 min at 600 rpm in preparation for the next elution cycle. Eluting magnetosomes were collected in 100 mL aliquots. After completing the last elution cycle the filter chamber was flushed copiously with 50 mM HEPES buffer pH 8.0 at 7.2 $L{\cdot}h^{-1}$ and 'zero field' without stirring. At the end of each run the filter was disassembled, visually inspected, and washed clean. The filter was then reassembled and cleaned-in-place with 20% (v/v) ethanol at 7.2 $L{\cdot}h^{-1}$ with the stirrer switched OFF in readiness for the next run. Fractions issuing from all runs were collected on ice. The volumes were recorded. Small aliquots from each were removed for immediate analysis of protein, iron and PHA contents, and preparation of samples for TEM, and the rest was stored at − 20 °C until required.

2.5. Further purification

2.5.1. Magnetically enhanced density separation (MEDS)

Pooled RS-HGMS 'condition 3′ eluate was employed for evaluation MEDS as a low-cost scalable alternative to lab-based sucrose density gradient centrifugation (2.5.2). Two different aqueous two-phase systems (ATPS) were explored for MEDS i.e.: a classical PEG/phosphate combination (120 $g{\cdot}L^{-1}$ PEG 8000 / 0.36 M K_2HPO_4 + 0.25 M KH_2PO_4, pH 8.0); and a micellar ATPS (15–20% w/v Eumulgin ES in 50 mM sodium phosphate, pH 7.0) that we have used previously for demonstration of a continuous magnetic extraction process (Fischer et al., 2013). Two and half millilitre samples were mixed with 10 mL of each ATPS contained in Falcon® 6-well (i.d. = 34.6 mm, depth = 20 mm) flat-bottom cell culture plates (Corning, B.V. Life Sciences, Amsterdam, The Netherlands), which were immediately sealed and placed on top of a powerful Nd-Fe-B permanent magnet block (1.32 – 1.37 T, 110 ×89 ×19.5 mm; Supermagnete) before transferring to an incubator (MaxQ™ 4000 Benchtop Model SHKE4000–8 C; Thermo Fisher Scientific, Loughborough, Leics, UK) without shaking, held at temperatures of 25 or 29 °C. One hour later the plate and magnet were carefully retrieved from the incubator and the separated phases were rapidly transferred (<5 min) into different containers for subsequent determination of iron, protein, and PHA contents, and preparation for TEM analysis.

2.5.2. Sucrose density gradient centrifugation

One millilitre samples of pooled RS-HGMS 'condition 3′ eluate were layered onto 4 mL cushions of 60% (w/v) sucrose in 10 mM HEPES buffer pH 8.0 contained in 10 mL Oak Ridge High-Speed PPCO screw-cap round-bottomed centrifuge tubes (Model 3119–0010, Thermo Fisher Scientific, Loughborough, Leics, UK), before centrifuging at 57,438 g_{max} in the fixed angle rotor 'model 12111′ (10 × 10 mL) of a Sigma 3–30KS high speed refrigerated centrifuge (Sigma Laborzentrifugen GmbH, Osterode am Harz, Germany) for 2.5 h at 4 °C. After centrifugation, the 'light' sucrose top phases were carefully removed using a Pasteur pipette, and 'heavy' magnetosome particles collected at the bottoms of the tubes, were resuspended in 10 mM HEPES buffer pH 8.0. Both phases were analysed for iron, protein, PHA and by TEM.

2.6. Analytical methods

Optical density and cellular magnetism (C_{mag}) of *M. gryphiswaldense* MSR-1 cultures were determined in a modified Evolution 300 UV-Vis spectrophotometer (Thermo Fisher Scientific, Loughborough, Leics, UK) at a wavelength of 565 nm. Data was collected using VISION*pro* software. Immediately after recording an OD_{565} value C_{mag} was measured on the same sample using a magnetic measurement system mounted within the spectrophotometer (Fernández-Castané et al., 2017, 2018). The system comprised two pairs of Helmholtz coils arranged around the cuvette holder, one pair in line with the light beam, the other orthogonal to it. Each set of coils is energized in turn, and the OD_{565} is recorded in each condition. Magnetic cells orient with the field; thus, recorded OD_{565} values change on switching the field orientation. Non-magnetic cells do not move, so OD_{565} remains the same. C_{mag} is calculated by ratioing the OD_{565} value measured when cells are aligned parallel to the light beam by that obtained when cells are aligned at 90° to the light beam.

Dry cell weight (DCW) measurements were performed in triplicate on 1 mL samples as described previously (Fernández-Castané et al., 2018).

Extents of cell disruption were determined by flow cytometry in a BD Accuri C6 flow cytometer (BD Biosciences, Wokingham, Berks, UK). Samples were resuspended in phosphate-buffered saline (PBS), stained with the DNA dye, SYTO™ 62 (Thermo Fisher Scientific, Loughborough, Leics, UK), and excited with a 640 nm solid-state laser. Fluorescence data was detected using a 675/25 BP filter as detailed earlier (Fernández-Castané et al., 2017).

Total protein contents were assayed using Pierce™ BCA Protein Assay Kits (Thermo Fisher Scientific, Loughborough, UK) and a Biochrom® Anthos Zenyth 340 microplate reader (Biochrom Ltd, Cambridge, Cambs, UK). Prior to analysis samples were mixed with an equal volume of 2 M NaOH and heated in a water bath at 100 °C for 10 min and then cooled to room temperature. Iron concentrations in samples were determined in a Perkin Elmer AAnalyst 300 Atomic Absorption Spectrometer (Waltham, MA, USA) using a single element iron (248.3 nm) hollow cathode lamp (SMI-LabHut Ltd., Churcham, Glos, UK) operated at a current of 30 mA with an acetylene (0.7 $L{\cdot}min^{-1}$) / air (4.0 $L{\cdot}min^{-1}$) flame. Samples were prepared in triplicate as described previously (Fernández-Castané et al., 2018, 2021; Heyen and Schüler, 2003). In some cases, samples were filtered through 0.2 μm filters to remove unbroken and fragmented cells and associated materials, e.g., unreleased magnetosomes and polyhydroxyalkanoate (PHA) granules, before assaying for iron and protein contents.

PHA content in samples was measured using a fluorescence-based assay (Fernández-Castané et al., 2017, 2018) adapted for use in microwell plates. Pyrromethene-546 (Pyr-546; Photonic solutions, Ohio, USA) working solution (0.1 $mg{\cdot}mL^{-1}$) was added to 20% (w/v) suspended cells in 50 mM HEPES buffer pH 8.0 prior to disruption to a final concentration of 2 $\mu g{\cdot}mL^{-1}$. Fluorescence was measured with Mithras LB 940 microplate reader (Berthold Technologies, Bad Wildbad, Germany) using 200 μL samples in Corning 96-well NBS microplates (Corning Life Sciences B.V., Amsterdam, The Netherlands).

Magnetic hysteresis loops of purified magnetosomes were recorded at room temperature in a MicroMag 2900 Alternating Gradient Magnetometer (PMC, Princeton, NJ, USA) between ± 1.0 T with an averaging time of 300 ms.

Cell pellets or magnetosome containing samples were prepared for TEM as described previously (Fernández-Castané et al., 2017, 2018, 2021). Briefly, this involved: (i) centrifugal recovery; (ii) fixing pelleted material in 2.5% (v/v) glutaraldehyde; (iii) exhaustive dehydration in a series of washing steps; (iv) infiltrating/embedding and curing pellets in resin; (v) cutting thin (120 nm) sections in a Ultramicrotome; and (v) examining cut sections in a JEOL 1200EX TEM electron microscope (Jeol Ltd, Akishima, Japan) operated at 80 kV, in the transmission mode, with the beam current at 60 μA. Average (L_{av}) and median (L_{50}) magnetosome chain lengths for each sample were determined from cumulative mass undersize distribution plots derived from analysis of TEM images (Fernández-Castané et al., 2021). At least 800 magnetosome units or 65 chains of magnetosomes were counted per sample. PHA granule sizes (long and short dimensions) were measured from the same TEM images.

3. Results and discussion

3.1. Magnetosome chain length influences C_{mag}

Magnetosome manufacture starts with their biosynthesis during fermentation. Alterations in fermentation parameters give rise to changes in the number and size of magnetosome chains within MTB, which in turn impact subsequent magnetosome downstream processing. It has been previously reported that: the magnetic response (C_{mag}) of *M. gryphiswaldense* MSR-1 cells depends on content and arrangement of magnetosomes (Schüler, 2008; Schüler, Baeuerlein, 1998; Schüler et al., 1995); maximum C_{mag} values occur before maximum biomass concentration is achieved (Fernández-Castané et al., 2018; Wang et al., 2016; Yang et al., 2013); higher C_{mag} values correspond to longer magnetosome chains (Katzmann et al., 2013); the length of magnetosome chains is influenced by changes in changing in oxygen tension and growth temperature (Katzmann et al., 2013); and growth phase (i.e., exponential vs. stationary) influences magnetosome chain length (Sun et al., 2008).

To characterise the best starting material to employ for magnetosome bioprocessing, we sampled *M. gryphiswaldense* MSR-1 at different time points (72, 113, 163 and 212 h) during a high cell density fermentation in which pH-stat mode and continuous culture were combined in successive stages. Growth was monitored by measuring OD_{565}, C_{mag} and intracellular iron content (Fig. 2a). TEM imaging and analysis were employed to determine size distributions of magnetosome chains and characteristic median chain lengths, L_{50} (Fig. 2b). C_{mag} values peaked during exponential phase (reaching 2.19 at 72 h), and steadily dropped thereafter (falling to 1.09 at 163 h), whilst intracellular iron content continued to track the OD_{565} into stationary phase (Fig. 2a). TEM analysis of *M. gryphiswaldens*e MSR-1 cells sampled during the fermentation show striking time dependent changes in cell shape, size and PHA content (Fig. 3).

At 72 h exponential phase cells are elongated and contain long magnetosome chains, but with increasing fermentation time the cells become shorter, develop a more rounded aspect, containing shorter magnetosome chains and much more PHA (large white inclusions). These observations are consistent with reports that the length of magnetosome chains tightly correlates with cell length (Staniland et al., 2010; Katzmann et al., 2011).

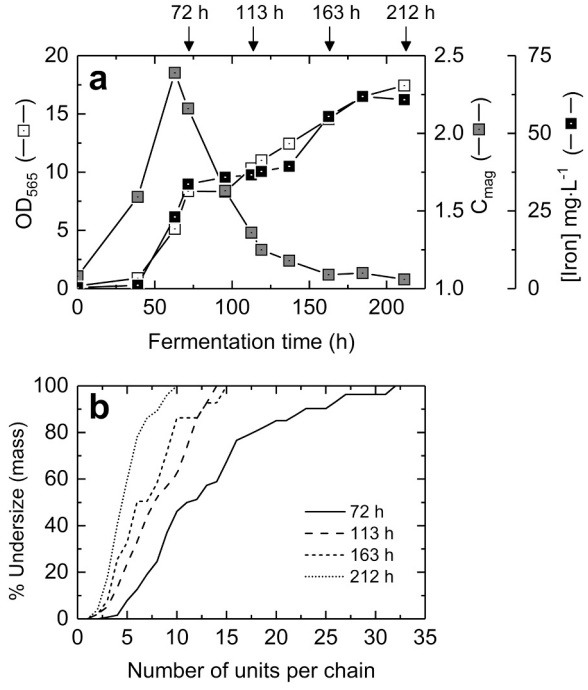

Fig. 2. Influence of fermentation time during two-stage continuous cultivation of *M. gryphiswaldense* MSR-1 (see Section 2.2) on: **(a)** OD_{565}, C_{mag}, and intracellular iron concentration; and **(b)** magnetosome chain length. At least 70 magnetosome chains were counted at each time point, and the size distributions are presented by plots of % cumulative mass undersize vs. number of units per chain.

3.2. Comparison of magnetosome release methods

Several small-scale mechanical methods have been employed for disruption of MTB, including French Pressing (Ginet et al., 2011; Gorby et al., 1988; Grünberg et al., 2001, 2004; Xiang et al., 2007), probe (Kobayashi et al., 2006) and bath-based ultrasound methods (Alphandèry et al., 2011, 2012), but little attention has been paid to comparative head-to-head evaluations of different methods on the basis of disruption efficiency and impact of the disruption process on the size distribution of released magnetosome chains.

In this study, we have performed a systematic examination of the disruption of *M. gryphiswaldense* MSR-1 cells with two lab-scale ultrasonic devices, i.e., an ultrasonic bath and a probe sonicator, and a Constant Systems Cell Disruptor (CSCD). The latter forces samples at high velocity through a specially designed disruptor head, and cells are disrupted by a combination of liquid shear, rapid pressure release, cavitation, elongational flow, and impingement (Lovitt et al., 2000; Middelberg, 1995). A wet cell concentration of 20% (w/v) used in previous reports (Grünberg et al., 2001; Lang and Schüler, 2008) was also employed in this work. Cell disruption efficiency before and after different disruption treatments was determined using flow cytometry to count the number of cells stained with the DNA dye, SYTO™ 62, per millilitre.

In initial studies pH-stat fed-batch fermented stationary phase *M. gryphiswaldense* MSR-1 cells (97 h, OD_{565} = 9.9, C_{mag} = 1.75) were used. CSCD disruption efficiency was tested at three different pressures (*P*) whilst varying the number of passes (*N*), and ultrasonic treatments were conducted for various times. Fig. 4a, b and c respectively show protein and iron release as functions of degree of cell disruption, and the dependencies of protein and iron release in the CSCD on variation in *P* and *N*. Release versus disruption efficiency data from all three devices collapsed along common curves (Fig. 4a). MSR-1 cell disruption and protein release (Fig. 4b) in the CSCD are first-order processes. For example, a single pass ($N = 1$) through the disruptor at 10 kpsi ruptured nearly 50% of the cells, two passes increased breakage to ~70%, and with every subsequent pass breakage increased further, reaching > 90% at $N = 5$. Evidently the release of magnetosomes (iron) from the cells is more complex (Fig. 4a & 4c). Two phases of release are discernible in Fig. 4a. In the first phase (5 – 70% disruption) iron release is substantially hindered cf. protein release, in the second phase (>70% disruption) becoming increasingly less so. This finding is understandable. Unlike much smaller sized proteins, the release of much larger magnetosome chains from damaged cells is likely hindered. However, increasing extents of disruption, e.g., multiple passes through the CSCD at higher pressures, (Fig. 4a) and concomitant reduction in chain length, remove this barrier and so facilitate magnetosome escape.

Figs. 5a and 5b compare size distributions of magnetosome chains before and after release from stationary and exponential phase MSR-1 cells by CSCD disruption at various combination of *P* and *N,* and Figs. 5c and 5d show derivative plots of median chain length, L_{50} measured in units, versus extent of disruption and *N*, respectively. Though the largest size of magnetosome chain in intact stationary phase cells was 23 units long, ~75% were below 15 units (Fig. 5a), and the median magnetosome chain length, L_{50} was 11.5 units (Fig. 5c & 5d). Exponential phase cells contained some longer magnetosome chains (20% between 17 and 32 units long; Fig. 5b), but the L_{50} of was slightly smaller than that of the stationary phase cells (i.e., 11 cf. 11.5; Fig. 5c & 5d). With increasing *P* and *N*, the size distribution curves gradually shifted left to smaller chains and became increasingly steep, providing

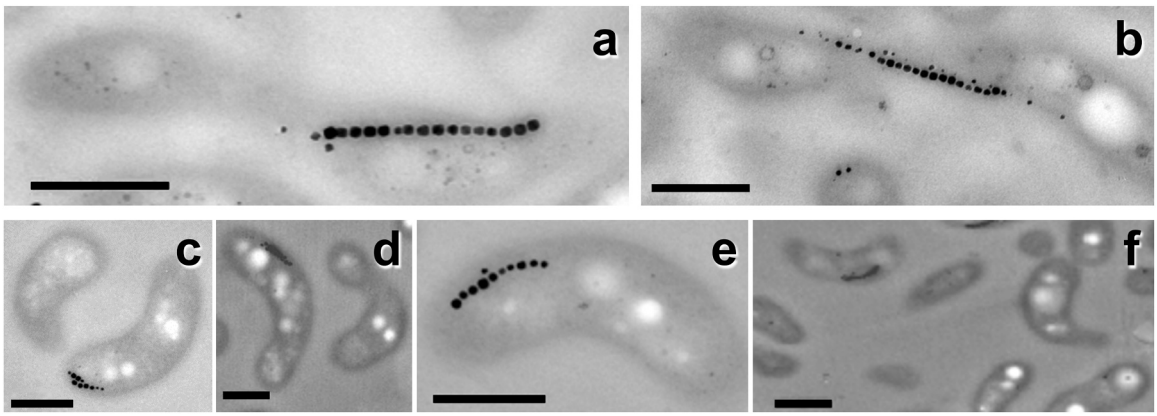

Fig. 3. TEM images of **(a, b)** exponential phase (72 h) and **(c-f)** stationary phase (163 h) *M. gryphiswaldense* MSR-1 cells. The scale bar is 0.5 μm.

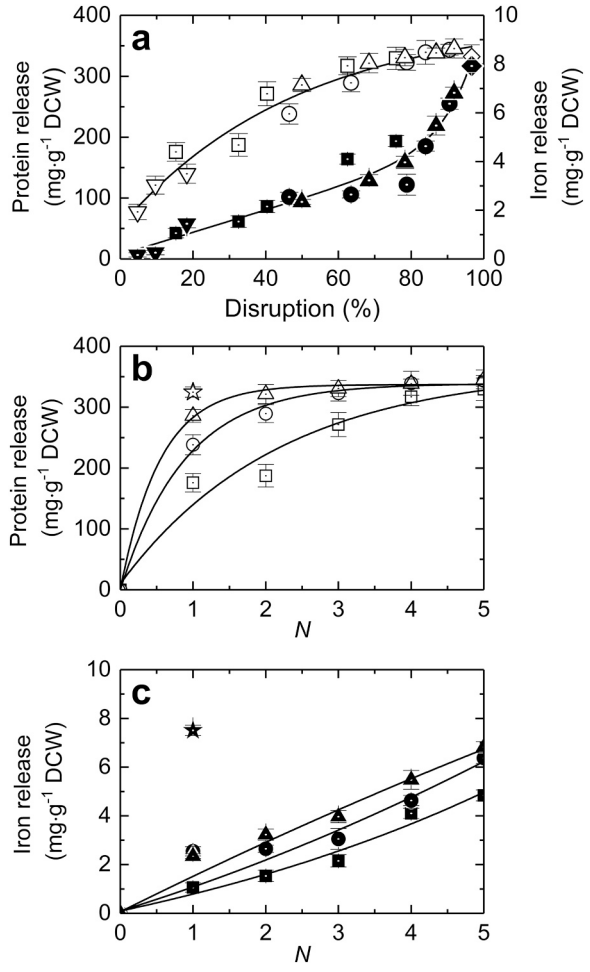

Fig. 4. (a) Protein and iron release vs. extent of disruption of stationary phase *M. gryphiswaldense* MSR-1 cells in all three devices. Protein **(b)** and iron **(c)** vs. *N* plots for the disruption of 20% (w/v) suspensions of stationary and exponential phase *M. gryphiswaldense* MSR-1 cells in the CSCD. Key: Protein (open symbols); iron (filled symbols); ultrasonic bath treatment of stationary phase cells (down-triangles); 10 min probe sonication of stationary phase cells (diamonds); 1 – 5 discrete passes of stationary phase cells through the CSCD at 5 kpsi (squares), 10 kpsi (circles) and 20 kpsi (up-triangles); and single pass of exponential phase cells through CSCD at 10 kpsi (stars).

clear evidence that chains of magnetosomes in intact cells were fractured into shorter and shorter chains during the cell disruption process.

Scrutiny of 'L_{50} vs disruption efficiency' plots (Fig. 5c) for stationary phase cells reveals a clear trend, i.e., increasing disruption efficiency leads to progressive reduction in median magnetosome chain length. Moreover, over the range of pressures used (5 – 20 kpsi) plots of 'L_{50} vs *N*' (Fig. 5d) imply chain degradation in the CSCD is a first-order process. To achieve efficient magnetosome recovery requires high disruption efficiencies of > 80%, but under such conditions the L_{50} drops from 11.5 units in the intact cell to below 5. Clearly, in the case of stationary phase cells there is a need to trade-off the degree of cell disruption and consequent recovery of magnetosomes from the cell against chain degradation inflicted during the disruption process. This does not apply to exponential phase cells, which proved much easier to disrupt likely reflecting a more elongated shape and weaker wall structures (Middelberg, 1995); i.e., one pass at 10 kpsi resulted in a disruption efficiency of 92% and small reduction in L_{50} from 11 (in intact cells) to 7.6 units long (Fig. 5c).

The quantities of iron (Fig. 4c) and protein (Fig. 4c) released from exponential phase cells in a single pass through the CSCD at 10 kpsi (7.5 ± 0.2 mg iron and 325 ± 8 mg protein per g DCW) matched those released from stationary phase cells exposed to 5 passes at twice the operating pressure (6.8 ± 0.2 mg iron and 346 ± 16 mg protein per g DCW), and the magnetosomes released were significantly larger; compare size distribution profiles (Fig. 5a & 5b), L_{50} values (Fig. 5c & 5d), and TEM images (Fig. 6).

Of the lab-based ultrasonic treatments previously used by others, 10 min of probe sonication delivered the most complete rupture of stationary phase cells (97%) releasing 87% of the magnetosomal iron (Fig. 4a) but inflicted the greatest damage on magnetosome chains reducing L_{50} to just 3.8 units (Fig. 5c), whilst 2 h in the ultrasonic bath released too few magnetosomes (16% of the total; Fig. 4a) from stationary phase cells for accurate size distribution analysis. For reasons of scalability, ease of disruption and reduced chain degradation, in all subsequent downstream process development work we employed exponential phase *M. gryphiswaldense* MSR-1 cells disrupted at 10 kpsi in a single pass through the CSCD.

3.3. Magnetosome recovery from CSCD homogenate by RS-HGMS

Magnetic-activated cell sorting (MACS) columns are plastic syringes filled with lacquered superparamagnetic beads. When used in conjunction with permanent magnets these separate magnetically labelled cells from non-magnetic cells by the principle of HGMS. Clinicians consider MACS systems the clinical benchmark for affinity separation and sorting of cells (https://www.miltenyibioindustry.com/en/platforms/clinimacs-prodigy-platform.html#gref).

Within the magnetosome research community MACS columns are also finding increasing favour over simple permanent bar magnets for the recovery of magnetosomes (Grünberg et al., 2004; Rosenfeldt et al., 2021; Uebe et al., 2011) at small lab scales. However, commercial MACS

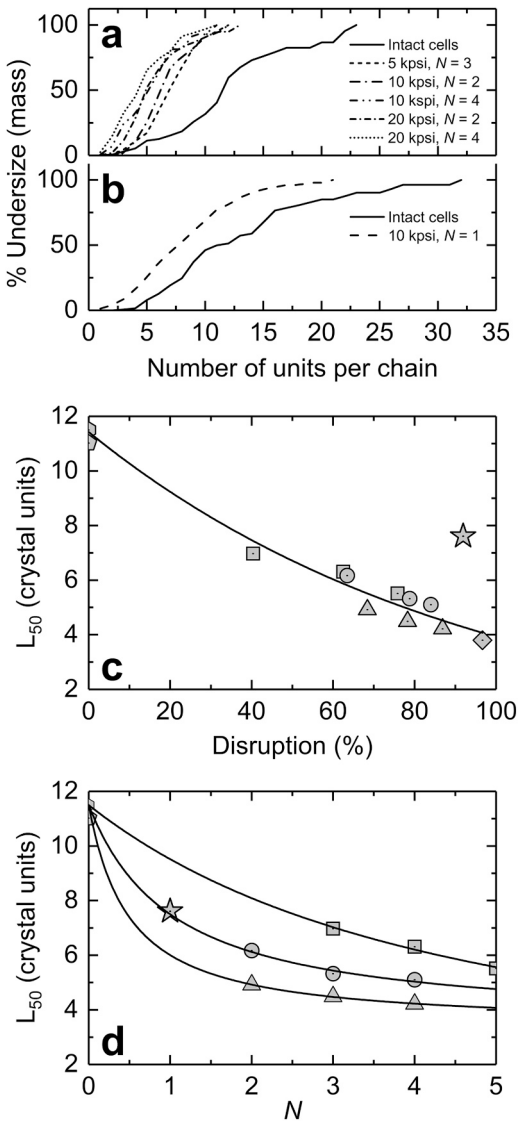

Fig. 5. Changes in magnetosome size distribution during disruption of **(a)** stationary and **(b)** exponential phase *M. gryphiswaldense* MSR-1 cells in the CSCD. At least 65 chains of magnetosomes were counted in each case. Plots of **(c)** L_{50} vs. extent of disruption and **(d)** L_{50} vs N for the disruption of *M. gryphiswaldense* MSR-1 cells in the CSCD. Key: Stationary phase cells (grey hexagon); stationary phase cells after 10 min of probe sonication (grey diamond); stationary phase cells after passes through the CSCD at 5 kpsi (grey squares), 10 kpsi (grey circles) and 20 kpsi (grey up-triangles); exponential phase cells after a single pass at 10 kpsi (grey star).

columns are not realistic prospects for large scale collection and partial purification of magnetosomes from concentrated cell homogenates. The small distances between the nonporous magnetic particles of MACS filters (~20 lymphocyte diameters or ~200 μm; https://www.miltenyibiotec.com/US-en/products/macs-cell-separation/columns/macs-columns-at-a-glance.html) render them acutely sensitive to fouling and blockage when challenged with dirty bioprocess feedstocks laden with sticky micronized materials such cell debris and PHA granules. Hence, common practices in lab-based magnetosome recovery schemes are to condition the disrupted cell extracts, either by subjecting them to low g spins and/or heavy dilution, prior to magnetic enrichment (Rosenfeldt et al., 2021). Neither practice fits the concept of an intensified downstream process for magnetosomes. While centrifugation preferentially sediments large PHA granules losses of co-sedimenting magnetosomes can be costly, e.g., Rosenfeldt and coworkers (2021) cite a ca. 40% loss of yield, and excessive dilution, especially at an early stage, results in poor process economics. Biomass accumulation within MACS filters impairs the recovery of magnetosomes from the filter at zero field, which limits their application to a single cycle of use. Moreover, the amount of magnetosomes that MACS cartridges can collect and subsequently release, on a per unit volume basis, is small.

The design of the small-scale fully automated RS-HGMS system employed in this work addresses many of the problems of MACS systems. Serious mechanical entrapment of biomass is avoided as the filter matrix comprises stainless-steel discs perforated with large '3 mm' diameter holes. Further, the rotor-stator design permits effective re-slurrying at zero field, so that weakly absorbed or entrained material can be removed from collected magnetic particles by washing steps conducted within the separator.

Table 1 presents summaries of magnetosome recovery and contaminant removal from crude cell homogenate by RS-HGMS using different loading and washing conditions. In all cases three sequential in situ washing cycles were conducted post loading, each with fresh buffer to dislodge loosely adsorbed and/or entrained species. OD_{560} measurements on exiting samples from all RS-HGMS runs with 250 mL portions of 20% (w/v) MSR-1 homogenates (72 h, 10 kpsi, $N = 1$) confirmed 2–3 washes were sufficient to remove freely suspended insoluble cell debris particulates from collected magnetosome cakes.

A high flowrate of 3.6 $L{\cdot}h^{-1}$ for both loading and washing steps (Table 1, condition 1; Fig. S1a & b) led to nearly 99% protein removal, i.e., 59.6% in the flowthrough and 39% in the wash. However, < 46% of the applied magnetosomes were retained in the filter post washing. 'Elution and flushing combined' recovered < 63% of these washed magnetosomes in substantially purified form with respect to protein ($PF_{Prot} = 6.3$); the remainder were trapped within the filter at the end of the experiment (mass balance closed to 79.1%).

When the flowrate for loading and washing was reduced to 0.6 $L{\cdot}h^{-1}$ (Table 1, condition 2; Fig. S1b & c) magnetosome losses dropped to just 0.5% and 9.5% respectively. Recoveries were high, i.e., 58.6% by elution alone and 70.6% overall (elution + flush), but contaminant removal was impaired (e.g., PF_{Prot} of 1.77 overall and 1.62 for elution).

The best compromise of recovery and purification was obtained when using low loading and high washing flowrates (Table 1, condition 3; Fig. 7). Virtually all (99.4%) of magnetosomes were recovered in the filter during loading, but little cleansing of the collected magnetosomes occurred at this stage. However, considerable purification of 'filter bound' magnetosomes was achieved during the washing steps ($PF_{Prot} = 3.47$, $PF_{PHA} = 1.12$), which removed a further 78% and 36% of the original protein and PHA respectively, at the expense of a 31.3% loss in magnetosome yield (mostly single crystal units and short chains, see later Section 3.5). Magnetosomes were subsequently recovered in > 52% yield in the elution fraction, in substantially purified form, i.e., > 4-fold and ~1.9-fold with respect to protein and PHA respectively.

In contrast, magnetosomes released from the filter by flushing (6%), and those remaining trapped (10.1%), though depleted in protein, were heavily enriched (~1.4 and 2.5-fold respectively) in PHA cf. the original feed. Scrutiny of Fig. 7 shows quite different concentration profiles for all three components (magnetosomes, protein, PHA) during RS-HGMS processing. While the vast bulk of protein eluted before the elution phase, most PHA tracked with magnetosomes. This explains why post-washing purification with respect to protein and PHA were respectively good (9.92-fold for elution fraction 5, 4.03-fold for elution pool) and comparatively poor (4.71-fold for elution fraction 4, 1.88-fold for elution pool).

The co-purification of adhesive PHA granules with magnetosomes during magnetic separation is known (Rosenfeldt et al., 2021). In their native in vivo state, the hydrophobic surface of PHA granules is protein coated (Bresan et al., 2016). PHA granule size was unaffected at all stages in magnetosome downstream processing (Table S1), but damage to their protein coats in vitro (especially during cell disruption) appears likely. In the event, exposed regions of sticky PHA polymer surface

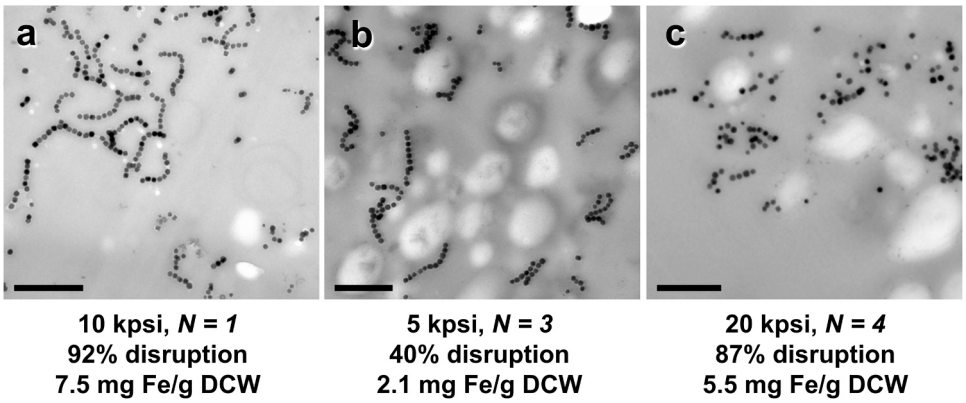

Fig. 6. TEM images of 72 h exponential **(a)** and stationary **(b & c)** phase *M. gryphiswaldense* MSR-1 cells following disruption in the CSCD. The text below each TEM shows the conditions applied (pressure and number of discrete passes), the extent of disruption and iron release per g dry cell weight. All scale bars indicate 0.5 μm.

Table 1
Summary of data for HGMS based recovery of magnetosomes from 250 mL portions of 20% (w/v) suspensions of CSCD disrupted ($P = 10$ kpsi, $N = 1$) exponential phase (72 h) MSR-1 cells. Flowrates used during loading and washing were either 0.6 or 3.6 L·h^{-1}. A flowrate of 7.2 L·h^{-1} was employed for all elution and flushing operations. Initial iron, protein and PHA concentrations in the feed were estimated as 428 ± 3 mg·L^{-1}, 15.1 ± 0.3 g·L^{-1} and 1.85 × 10^9 RFU·L^{-1} respectively. Key: PF_{Prot} = purification factor with respect to protein; PF_{PHA} = purification factor with respect to PHA.

Condition 1: Loading & washing @ 3.6 L·h^{-1}			
Pooled fractions	Iron (%)	Protein (%)	PF_{Prot} (-)
Flow-through	36.8 ± 0.6	59.6 ± 1.7	0.62
Wash	17.3 ± 0.9	39.0 ± 2.6	0.44
Elution	22.0 ± 1.0	3.3 ± 0.3	6.67
Flush	3.1 ± 0.2	0.7 ± 0.02	4.52
Mass balance	*79.2*	*102.7*	
Condition 2: Loading & washing @ 0.6 L·h^{-1}			
Pooled fractions	Iron (%)	Protein (%)	PF_{Prot} (-)
Flow-through	0.5 ± 0.02	1.6 ± 0.1	0.29
Wash	9.5 ± 0.1	61.6 ± 3.0	0.15
Elution	58.6 ± 0.7	36.2 ± 1.8	1.62
Flush	12.0 ± 0.3	3.7 ± 0.2	3.22
Mass balance	*80.6*	*103.1*	

Condition 3: Loading @ 0.6 L·h^{-1} & washing @ 3.6 L·h^{-1}					
Pooled fractions	Iron (%)	Protein (%)	PF_{Prot} (-)	PHA (%)	PF_{PHA} (-)
Flow-through	0.6 ± 0.02	2.4 ± 0.1	0.23	3.1 ± 0.02	0.19
Wash	31.3 ± 0.8	78.0 ± 2.7	0.40	35.9 ± 0.8	0.87
Elution	52.1 ± 2.3	12.9 ± 0.7	4.03	27.6 ± 0.8	1.88
Flush	6.0 ± 0.2	2.2 ± 0.1	2.75	8.3 ± 0.1	0.72
Mass balance	*89.9*	*95.6*		*74.9*	

would be expected to interact with e.g., membrane phospholipids (Bresan et al., 2016; Griebel et al., 1968) of magnetosomes and potentially other species (e.g., non-magnetosome proteins, fine cell debris). The sticky nature of in vitro PHA is exemplified by the observation that ~25% of that applied to the filter in the feedstock remained in the filter at the end of the experiment cf. 10% of the iron and 4% of the protein (Table 1, condition 3).

3.4. PHA removal from RS-HGMS recovered magnetosomes by MEDS

Removal of contaminating PHA from magnetosomes is typically conducted by sucrose density gradient ultracentrifugation (Grünberg et al., 2001; Rosenfeldt et al., 2021). In the majority of cases, this is done by centrifuging heavy magnetosomes at 4 °C through a 60% (w/v)

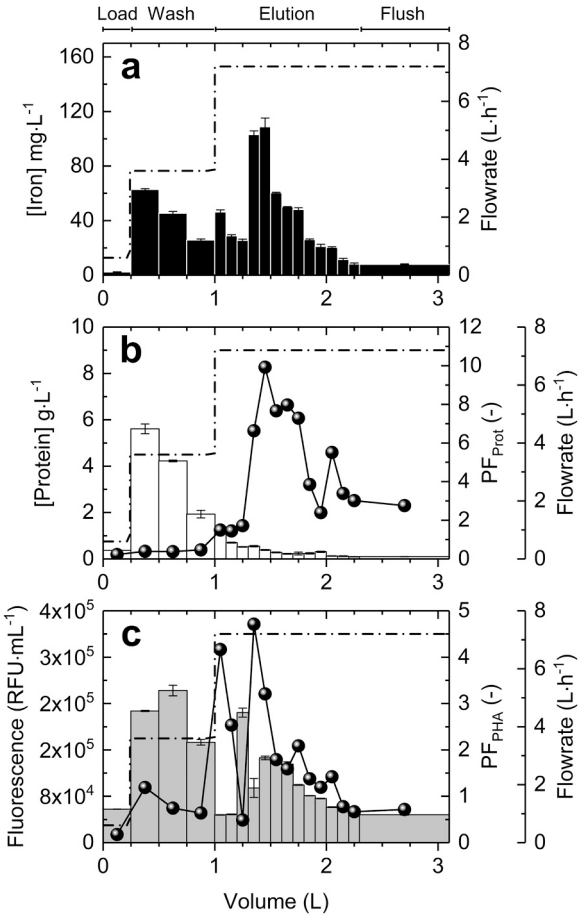

Fig. 7. RS-HGMS processing (condition 3) of crude 20% (w/v) CSCD (10 kpsi, $N = 1$) disrupted 72 h exponential phase *M. gryphiswaldense* MSR-1 cells. The panels show tracking of **(a)** iron (black bars), **(b)** protein (white bars), and **(c)** PHA (grey bars). The dot-dash lines in all plots show the flowrates used at each stage, and the spheres superimposed on bar charts **b** and **c** respectively indicate the PF_{Prot} and PF_{PHA} recorded for each fraction. See Table 1 and text for details.

sucrose cushion that retains the lighter suspended particulates, PHA granules and residual micronized cell debris, at equivalent centrifugation times, $Gt = t(\omega^2 R_0/g)$, in excess of 4 × 10^5 h (Rosenfeldt et al., 2021) where R_0 is the characteristic radius, ω is the angular velocity, t is the time; and g is the gravitational force. Performance is strongly influenced by material loading per tube and complete elimination of PHA from a sample may require extreme Gt values (33.6 × 10^5 h)

(Grünberg et al., 2001), or multiple sequential centrifugal runs at the much lower *Gt* (1.44×10^5 h) used in this work. The use of conventional tube rotor ultracentrifuges for large-scale density-based purification of magnetosomes is clearly untenable. Sophisticated continuous flow high speed zonal industrial ultracentrifuges (e.g., Alfa Wasserman KII, himac CC40NX) on the other hand, though potentially attractive for this application (Meriño, Glanzman, 2016; Morita et al., 2011), are expensive.

In this work, we have a sought a practical low-cost solution that simultaneously exploits the magnetic properties of magnetosomes and low density of PHA granules. In so-called 'magnetically enhanced density separation (MEDS)', the ultra-high centrifugal driving forces employed in density gradient ultracentrifugation are replaced with those of magnetic attraction, and the dense sucrose cushion is exchanged with an aqueous micellar two-phase system (AMTPS) previously employed for continuous flow magnetic extraction of proteins at technical scale (Fischer et al., 2013). Lighter PHA partitions into the lower density top phase whilst heavier magnetosomes are pulled into the denser bottom phase by a powerful NdFeB magnet block. PHA removal achieved by various MEDS treatments is summarised in Table 2 and compared with sucrose density gradient centrifugation.

The first trials of PHA removal by MEDS were conducted using the PEG8000/phosphate ATPS (Table 2) described by Divyashree et al., 2009 for the isolation of PHA from lysates of *Bacillus flexus*. Less than 44% of magnetosomes present in the pooled RS-HGMS eluate were pulled into the highly dense (1350 $kg{\cdot}m^{-3}$) bottom phase along with 7.6% of the PHA; the residual PHA (92.4%) remained in the PEG-rich top phase. Ten-fold sample dilution only marginally improved magnetosome recovery (54.1%) and purity (7.5% PHA & $PF_{PHA} = 7.21$) in the bottom phase. Evidently the 1.35 T magnet block was not strong enough to drag magnetosomes in high yield into the overly dense (1350 $kg{\cdot}m^{-3}$) bottom phase.

In stark contrast, the same magnet proved highly effective when used in combination with the Emulugin ES AMTPS (Table 2). AMTPS are markedly different from classical ATPS, as they feature non-ionic surfactants predisposed to separate from a single-phase regime to two-phase regime in response to a change in temperature (Becker et al., 2009; Fischer and Franzreb, 2011, 2012; Fischer et al., 2013; Galaev and Mattiasson, 1993). In the experiments conducted here, pooled eluate was mixed with 15 or 20% (w/w) Eumulgin ES in 50 mM sodium phosphate pH 7.0, at ~21 °C (i.e., in the single-phase regime) before placing on the magnet block and raising the temperature to 25 or 29 °C (two-phase regime) to induce phase separation. The top and bottom phase surfactant concentrations were respectively estimated from the coexistence curve for Eumulgin ES in 50 mM sodium phosphate, pH 7.0 (Fischer et al., 2013) as 21.7% and 3.8% (w/w) at 25 °C, and 47.3% and 0.3% (w/w) at 29 °C.

Under all conditions examined the magnetosomes were pulled in high yield (87.6 – 97.7%) into the micelle-poor bottom phases, while most PHA granules (62.6 – 89.2%) separated into in the micelle-rich upper phases. Losses of magnetosomes (2 –10%) and PHA (15.7–31.2%) to the interface were observed at 25 °C, i.e., very close to the cloud point temperature (24.5 °C) for the Emulugin ES – 50 mM sodium phosphate pH 7.0 system (Fischer et al., 2013), but were eradicated for magnetosomes and approximately halved for PHA (6.8 – 15.7%) at 29 °C. Remarkably clean separation was achieved by MEDS in 15% (w/w) Emulugin ES at 29 °C, i.e., > 96% of the magnetosome product was recovered in the bottom phase in 24.1-fold purified form with respect to PHA (Table 2, Fig. S2). Inferior magnetosome yields and purities were achieved by MEDS in 12% PEG/phosphate at 28 °C and by centrifugation through a 60% sucrose cushion at 4 °C and *Gt* $= 1.44 \times 10^5$ h (see Table 2). Note, had much higher *Gt* values been employed for centrifugation (Grünberg et al., 2001; Rosenfeldt et al., 2021) magnetosome recoveries and purities similar or greater than those achieved by MEDS in 15% (w/w) Emulugin ES at 29 °C would have been recorded. However, in contrast to ultracentrifugation, MEDS inherits two key advantages of ATPS/AMTPS namely, facile scale-up and potential for continuous operation (Espitia-Saloma et al., 2014; Fischer et al., 2013; Ruiz-Ruiz et al., 2019; Trakultamupatam et al., 2004a, 2004b). Use of Eumulgin ES and moderate temperatures has the added benefit of eliminating the high costs associated with phase forming components (Becker et al., 2009; Fischer and Franzreb, 2012; Fischer et al., 2013; Oelmeier et al., 2011). Apparatus for continuous MEDS should be relatively easy to construct; for example, likely comprising a temperature-controlled mixer configured with a flowthrough separation chamber (settler) housed in a tailor-made permanent magnet yoke. Indeed, we employed a similar rig to demonstrate continuous protein purification using magnetic nanoparticle adsorbents in the same AMTPS, i.e., Eumulgin ES (Fischer et al., 2013).

The superior separation of PHA and magnetosomes from one another by MEDS in the Eumulgin ES AMTPS cf. PEG8000-phosphate ATPS can, in large part, be attributed to differences in the buoyant densities of the bottom phases and densities of PHA granules and magnetosomes. Reported values for the density of bacterial PHA biopolymers range from as low as 1000 $kg{\cdot}m^{-3}$ for medium-chain-length PHA granules of low crystallinity (Van Hee et al., 2004, 2006) to 1250 $kg{\cdot}m^{-3}$ for highly crystalline polyhydroxybutyrate (Cherpinski et al., 2017). The observation here, for MEDS-AMTPS, that only 4–10% of PHA entered the 1070 – 1090 $kg{\cdot}m^{-3}$ bottom phase and 63 – 89% resided in the 940 – 970 $kg{\cdot}m^{-3}$ top phase (Table 2) implies an 'apparent' density for the PHA granules processed from MSR-1 of close to 1000 $kg{\cdot}m^{-3}$. While the buoyancy of the dense (1350 $kg{\cdot}m^{-3}$) bottom phase of the PEG/phosphate ATPS provided strong resistance to the 1.37 T permanent magnet's pull on the heavier magnetic magnetosome (Table 2), the density (1070 – 1090 $kg{\cdot}m^{-3}$) of the bottom phase of Eumulgin ES lies in an operational 'sweet-spot' for MEDS; i.e., it is light enough to allow most

Table 2
Comparison of MEDS-ATPS, MEDS-AMTPS and sucrose density gradient centrifugation for the separation of PHA from magnetosomes. HGMS eluate was further separated by MED-ATPS (12% w/v PEG8000 in 0.36 M K_2HPO_4 + 0.25 M KH_2PO_4, pH 8.0), MEDS-AMTPS (15 or 20% w/w Eumulgin ES in 50 mM sodium phosphate, pH 7.0), and density gradient centrifugation through a 60% (w/v) sucrose cushion in 10 mM HEPES buffer pH 8.0. All recoveries are expressed as percentages of the total recovered. Key: R = volume ratio (top/bottom) of system; R_{exp} = volume ratio (top/bottom) in experiment; PF_{PHA} = purification factor with respect to PHA.

MEDS system	T (°C)	Density ($kg{\cdot}m^{-3}$)		R (-)	Volume (%)			R_{exp} (-)	Top (%)		Interf. (%)		Bottom (%)		PF_{PHA} (-)
		Top	Bottom		Top	Interf.	Bottom		Iron	PHA	Iron	PHA	Iron	PHA	
12% PEG/phosphate	28	1030	1350	0.77	43.5	-	56.5	0.77	56.3	92.4	0.0	0.0	43.7	7.6	5.75
15% Emulugin ES	25	960	1090	0.47	32.0	2.2	65.8	0.49	10.3	75.5	2.0	15.7	88.7	8.8	10.08
20% Emulugin ES	25	950	1070	0.94	42.9	5.5	51.6	0.83	2.4	62.6	10.0	31.2	87.6	6.2	14.13
15% Emulugin ES	29	970	1080	0.28	21.9	1.0	77.1	0.28	3.7	89.2	0.0	6.8	96.3	4.0	24.08
20% Emulugin ES	29	940	1070	0.67	35.0	2.0	63.0	0.56	2.3	74.2	0.0	15.7	97.7	10.1	9.67

Sucrose density gradient centrifugation	Retained (%)		Sedimented (%)		PF_{PHA} (-)
	Iron	PHA	Iron	PHA	
57,438 g_{max}, 2.5 h, 4 °C ($Gt = 1.44 \times 10^5$ h)	28.3	89.2	71.7	10.8	6.64

(88 – 98%) magnetosomes to be magnetically pulled into it, whilst simultaneously providing enough upthrust on PHA particles to exclude most (90 – 96%) of them (Table 2). The much smaller density differential between the top and bottom phases of Emulugin ES – AMTPS (110 – 130 kg·m^{-3}) cf. PEG/phosphate ATPS (330 kg·m^{-3}) and poor performance of the latter system with samples of higher dirt load, e.g., directly after cell disruption (Y_{Fe} = 16.2%, Y_{PHA}= 9.6%; PF_{PHA}=1.69) does not encourage testing of MEDS-AMTPS pre-RS-HGMS. We envisage RS-HGMS playing a capture and partial purification role and that MEDS-AMTPS is reserved for polishing.

3.5. Changes in magnetosome size and magnetic properties during DSP

Our original aim was to develop a scalable recovery process for magnetosome products that retained much of their unique chain and magnetic characteristics. Fig. 8a shows changes in size distribution at every stage in the process. Not surprisingly, the biggest reduction in chain length was inflicted by CSCD (L_{50} dropped from 11.5 to 7.7), the first step in the process. In the second, RS-HGMS (condition 3), loss of smaller and less magnetic chains during the loading phase raised L_{50} to 9.5. Following MEDS L_{50} fell to 7.2. In part, this reduction can be explained by loss of some larger chains (e.g., 16–21 units long) to the top phase, likely via association with sticky PHA granules; but given the high recovery achieved in the bottom phase (>96%) a small degree of fragmentation also seems plausible. TEM analysis (Fig S2c) however, shows no evidence of MEDS induced damage to magnetosome chains of the types induced by ultrasonication or exposure to SDS (Fernández-Castané et al., 2021). These treatments are known to denature the MamK filament (Scheffel et al., 2006), dissociate magnetosome from chains, and disrupt the magnetosome membrane (Alphandéry et al., 2012), collectively inducing chain collapse and agglomeration into compact structures (Alphandéry et al., 2012, 2013).

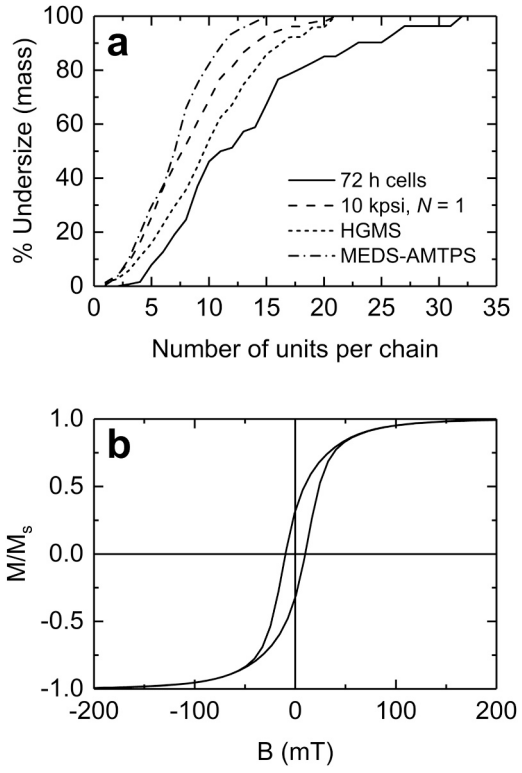

Fig. 8. (a) Changes in magnetosome size during different points in DSP. **(b)** Normalised room temperature magnetic hysteresis loop of purified magnetosomes after the final MEDS-AMTPS step (15% w/w Emulugin ES – 50 mM sodium phosphate pH 7.0, 29 °C).

Based on L_{50} values roughly 65% of the original in vivo magnetosome chain length was retained.

Fig. 8b shows normalised magnetic hysteresis loop for purified magnetosomes at room temperature. The loop is closed at ~50 mT, saturated at low field < 200 mT and displays the familiar distorted pot-bellied shaped hysteresis loop reported by others for whole MTB (Denham et al., 1980; Gehring et al., 2012; Katzmann et al., 2013; Kumari et al., 2015; Li et al., 2010; Moskowitz et al., 1988; Zhang and Pan, 2018) and isolated magnetosomes (Denham et al., 1980; Li et al., 2010). Standard hysteresis values for coercivity (B_c = 9.8 mT), remanent coercivity (B_{cr} = 18.1 mT), B_{cr}/B_c (1.85) and 'squareness' (M_{rs}/M_s = 0.32) are very similar to those reported by Li et al. (2010) for magnetosomes isolated from *M. magneticum* AMB-1, and by Zhang and Pan (2018) for whole *M. gryphiswaldense* MSR-1 cells (Table S3). The lower squareness and B_c (ca. 15–35% reduced) and higher B_{cr}/B_c ratios (ca. 15–40% higher) of extracted and purified MSR-1 magnetosome chains cf. whole *M. gryphiswaldense* MSR-1 cells (Table S2) are not unexpected. They stem from a combination of: (i) strong magnetic interactions between chains (Denham et al., 1980; Moskowitz et al., 1988) which are absent between magnetic cells which behave as non-interacting SD particles; (ii) decreased intrachain interactions cf. anchored chains in cells (Li et al., 2010); (iii) reduced chain length, which correlates with reduction in B_c (Moskowitz et al., 1988; Zhang and Pan, 2018); and (iv) physico-chemical time-dependent changes to the composition of the magnetic cores of magnetosomes on exposure to oxic environments (Fischer et al., 2011; Gehring et al., 2012). Biogenic magnetite in magnetosome chains is structurally pure but following release from cells into an oxic environment magnetosome magnetite undergoes slow topotactic transition to maghemite, γ–Fe_2O_3 (Fischer et al., 2008, 2011; Gehring et al., 2012), and conceivably, given sufficient time can undergo further partial oxidisation to paramagnetic hematite, α–Fe_2O_3 (Cornell and Schwertmann, 2003; Zheng et al., 2021). The magnetosome membrane retards (Kumari et al., 2015), but cannot prevent, significant surface-controlled oxidation of the encased magnetic crystals from occurring. For example, Mickoleit et al., 2023 reported that purified magnetosome suspensions lost two-thirds of their saturation magnetisation within 1 year when stored at 4 °C under nitrogen, and that the rate of decay was ca. 10 × faster when stored at room temperature under air.

3.6. Process summary

Table 3 summarises key data for the proposed downstream process for magnetosomes from exponential phase cells. A single pass through the CSCD disrupted 92% of the cells releasing 75% of the cellular iron. Step yields for the subsequent RS-HGMS and MEDS steps were 70% and 96% respectively. Magnetosomes were recovered in > 50% yield purified ca. 50 and 80-fold with respect to PHA and protein respectively. The 250 mL rotor-stator separator used in this work is much smaller than cGMP compliant (Ebeler et al., 2018) commercial variants available from Andritz Separation GmbH (https://www.andritz.com/products-en/group/separation/disc-drum-filters/hgms-high-gradient-magnetic-separator), but is nevertheless oversized for the work performed here with magnetosomes. The filter was challenged with magnetosome loadings equivalent to ~0.15 g of magnetite, but from particle breakthrough experiments performed with various magnetic particles, we know this filter can handle much more than this, i.e., > 25 g of M-PVA supports (ca. 2 μm diameter), the equivalent of > 8 g of magnetite, while Krolitzki et al. (2023), using a similarly sized RS-HGMS (MES-25 RS, Andritz KMPT GmbH, Germany) determined capacities in excess of 40 g for sub 20 nm magnetic nanoparticle adsorbents (equivalent to >20 g of magnetite). Substantially increasing magnetosome loadings per unit filter volume is expected to improve separator performance overall, importantly allowing concentration of the recovered magnetosomes in the elution pool cf. the crude feedstock.

Table 3
Summary of key data for the downstream processing of magnetosomes from MSR-1 cells. Key: Y_{Fe} = iron yield; Y_{Prot} = Protein yield; Y_{PHA} = PHA yield; PF_{Prot} = purification factor with respect to protein; PF_{PHA} = purification factor with respect to PHA.

Process stage	Y_{Fe} (%)		Y_{Prot} (%)		Y_{PHA} (%)		PF_{Prot} (-)		PF_{PHA} (-)	
	Step	Process	Step	Process	Step	Process	Step	Process	Step	Process
Exponential phase (72 h) cells	100	100	100	100	100	100	1.0	1.0	1.0	1.0
CSCD (10 kpsi, $N = 1$)	74.5	74.5	91.5	91.5	-	-	0.8	0.8	-	-
HGMS (condition 3, eluate)	70.0	52.1	14.1	12.9	-	27.6	5.0	4.0	-	1.9
MEDS (15% Eumulgin ES, 29 °C, bottom phase)	96.3	50.2	5.0	0.6	4.0	1.1	19.3	77.7	24.1	45.4

4. Conclusions

The overarching aim of this study has been to advance a scalable platform for the future production and purification of magnetosomes from *M. gryphiswaldense* MSR-1 and, by extension, other MTB. The platform comprises the following linked steps: two-stage continuous fermentation of MTB; centrifugal recovery of the cells; cell disruption to release the magnetosome chains; subsequent capture and partial purification of the magnetosomes in a RS-HGMS; and finally, purification/polishing of the magnetosomes free of PHA granules using MEDS, a new technique developed herein, inspired by our previous work on protein purification with magnetic adsorbents in micellar aqueous two-phase systems (Becker et al., 2009; Fischer et al., 2013).

Specifically, we have shown that: (i) maximum cellular magnetism, long magnetosome chain lengths and lower PHA contents are favoured during the exponential phase of growth; (ii) exponential phase cells are much easier to break cf. stationary phase (a single pass through the CSCD at moderate pressure ensures efficient magnetosome release with minimal attritive damage); (iii) effective use of a 'state-of-art' RS-HGMS for magnetosome recovery and partial purification from unclarified cell disruptates of high dirt load that block MACS columns; and finally (iv) MEDS is a viable scalable alternative to sucrose density gradient centrifugation for removing stubborn PHA granule impurities from magnetosome preparations.

In its current unoptimised form the process delivered a magnetosome yield of > 50% whilst removing 99% and 99.5% of the original PHA and protein contents. For future intensified manufacture of magnetosomes it is necessary that rapid upstream advances, such as higher yielding strains, pre-functionalised magnetosomes, autocatalytic depolymerisation of PHA to name but a few, are met with parallel development of bioprocess separation technology specifically tailored to the unique challenges they pose, rather than repurposing equipment designed for very different entities. The disclosed platform is promising in this respect but requires further work. A down-scaled approach, with much smaller RS-HGMS or new magnetic chromatography (Kuger et al., 2022) devices, and appropriately sized MEDS systems, seems appropriate for integrated process development and technical demonstration in batch and continuous modes.

CRediT authorship contribution statement

T.W.O. and O.R.T.T. conceptualized the study; A.F.C., H.L. and M.E. performed the experiments; M.F., T.W.O. and O.R.T.T. supervised the project; O.R.T.T. wrote the manuscript; A.F.C., M.F., T.W.O. and O.R.T.T proofread and approved the manuscript.

Declaration of Competing Interest

The authors declare that they have no known competing financial interests or personal relationships that could have appeared to influence the work reported in this paper.

The author Owen R.T. Thomas is also an Editor of the journal Food and Bioproducts Processing, however he was not involved in the peer review or handling this paper. The paper was handled by the Editor Marcello Fidaleo.

Acknowledgments

This work was supported by the ERA-IB grant EIB.13.016 ProSeCa, funded by the UK Biotechnology & Biological Sciences Research Council (BBSRC) as grant BB/M00483X/1. The authors acknowledge the expert technical assistance of Theresa Morris and Paul Stanley of the University of Birmingham's Centre for Electron Microscopy.

Appendix A. Supporting information

Supplementary data associated with this article can be found in the online version at doi:10.1016/j.fbp.2024.01.005.

References

Ali, A., Zafar, H., Zia, M., ul Haq, I., Phull, A.R., Ali, J.S., Hussain, A., 2016. Synthesis, characterization, applications, and challenges of iron oxide nanoparticles. Nanotechnol. Sci. Appl. 9, 49–67. https://doi.org/10.2147/NSA.S99986.

Ali, A., Shah, T., Ullah, R., Zhou, P., Guo, M., Ovais, M., Tan, Z., Rui, Y., 2021. Review on recent progress in magnetic nanoparticles: synthesis, characterization, and diverse applications. Front. Chem. 9, 629054 https://doi.org/10.3389/fchem.2021.629054.

Alphandéry, E., 2020. Bio-synthesized iron oxide nanoparticles for cancer treatment. Int. J. Pharm. 586, 119472 https://doi.org/10.1016/j.ijpharm.2020.119472.

Alphandéry, E., Faure, S., Seksek, O., Guyot, F., Chebbi, I., 2011. Chains of magnetosomes extracted from AMB-1 magnetotactic bacteria for application in alternative magnetic field cancer therapy. ACS Nano 5, 6279–6296. https://doi.org/10.1021/nn201290k.

Alphandéry, E., Guyot, F., Chebbi, I., 2012. Preparation of chains of magnetosomes, isolated from *Magnetospirillum magneticum* strain AMB-1 magnetotactic bacteria, yielding efficient treatment of tumors using magnetic hyperthermia. Int. J. Pharm. 434, 444–452. https://doi.org/10.1016/j.ijpharm.2012.06.015.

Alphandéry, E., Chebbi, I., Guyot, F., Durand-Dubief, M., 2013. Use of bacterial magnetosomes in the magnetic hyperthermia treatment of tumours: a review. Int. J. Hyperther. 29 (8), 801–809. https://doi.org/10.3109/02656736.2013.821527.

Bazylinski, D.A., Garratt-Reed, A.J., Frankel, R.B., 1994. Electron microscopic studies of magnetosomes in magnetotactic bacteria. Microsc. Res. Tech. 27 (5), 389–401. https://doi.org/10.1002/jemt.1070270505.

Becker, J.S., Thomas, O.R.T., Franzreb, M., 2009. Protein separation with magnetic adsorbents in micellar aqueous two-phase systems. Sep. Purif. Technol. 65 (1), 46–53. https://doi.org/10.1016/j.seppur.2008.05.017.

Ben-Shimon, S., Stein, D., Zarivach, R., 2021. Current view of iron biomineralization in magnetotactic bacteria. J. Struct. Biol.: X 5, 100052. https://doi.org/10.1016/j.yjsbx.2021.100052.

Berny, C., Le Fèvre, R., Guyot, F., Blondeau, K., Guizonne, C., Rousseau, E., Bayan, N., Alphandéry, E., 2020. A method for producing highly pure magnetosomes in large quantity for medical applications using *Magnetospirillum gryphiswaldense* MSR-1 magnetotactic bacteria amplified in minimal growth media. Front. Bioeng. Biotechnol. 8, 16. https://doi.org/10.3389/fbioe.2020.

Blakemore, R., 1975. Magnetotactic bacteria. Science 190 (4212), 377–379. https://doi.org/10.1126/science.170679.

Borg, S., Rothenstein, D., Bill, J., Schüler, D., 2015. Generation of multishell magnetic hybrid nanoparticles by encapsulation of genetically engineered and fluorescent bacterial magnetosomes with ZnO and SiO_2. Small 11, 4209–4217. https://doi.org/10.1002/smll.201500028.

Boucher, M., Geffroy, F., Prévéral, S., Bellanger, L., Selingue, E., Adryanczyk-Perrier, G., Péan, M., Lefèvre, C.T., Pignol, D., Ginet, N., Mériaux, S., 2017. Genetically tailored magnetosomes used as MRI probe for molecular imaging of brain tumor. Biomaterials 121, 167–178. https://doi.org/10.1016/j.biomaterials.2016.12.013.

Bresan, S., Sznajder, A., Hauf, W., Forchhammer, K., Pfeiffer, D., Jendrossek, D., 2016. Polyhydroxyalkanoate (PHA) granules have no phospholipids. Sci. Rep. 6 (1), 1–13. https://doi.org/10.1038/srep26612.

Brown, G.N., Müller, C., Theodosiou, E., Franzreb, M., Thomas, O.R.T., 2013. Multi-cycle recovery of lactoferrin and lactoperoxidase from crude whey using fimbriated high-capacity magnetic cation exchangers and a novel "rotor-stator" high-gradient magnetic separator. Biotechnol. Bioeng. 110, 1714–1725. https://doi.org/10.1002/bit.24842.

Cherpinski, A., Torres-Giner, S., Cabedo, L., Lagaron, J.M., 2017. Post-processing optimization of electrospun submicron poly (3-hydroxybutyrate) fibers to obtain

continuous films of interest in food packaging applications. Food Addit. Contam. Part A 34 (10), 1817–1830. https://doi.org/10.1080/19440049.2017.1355115.
Cornell, R.M., Schwertmann, U., 2003. The iron oxides: structure, properties, reactions, occurrences, and uses (Vol. 664). Weinheim: Wiley-VCH. https://doi.org/10.1515/CORRREV.1997.15.3–4.533.
Denham, C., Blakemore, R., Frankel, R., 1980. Bulk magnetic properties of magnetotactic bacteria. IEEE Trans. Magn. 16 (5), 1006–1007. https://doi.org/10.1109/TMAG.1980.1060821.
Divyashree, M.S., Shamala, T.R., Rastogi, N.K., 2009. Isolation of polyhydroxyalkanoate from hydrolyzed cells of *Bacillus flexus* using aqueous two-phase system containing polyethylene glycol and phosphate. Biotechnol. Bioprocess Eng. 14, 482–489. https://doi.org/10.1007/s12257-008-0119-z.
Ebeler, M., Pilgram, F., Wolz, K., Grim, G., Franzreb, M., 2018. Magnetic separation on a new level: Characterization and performance prediction of a cGMP compliant "rotor-stator" high-gradient magnetic separator. Biotechnol. J. 13, 1700448 https://doi.org/10.1002/biot.201700448.
Espitia-Saloma, E., Vázquez-Villegas, P., Aguilar, O., Rito-Palomares, M., 2014. Continuous aqueous two-phase systems devices for the recovery of biological products. Food Bioprod. Process. 92, 101–112. https://doi.org/10.1016/j.fbp.2013.05.006.
Fernández-Castané, A., Li, H., Thomas, O.R.T., Overton, T.W., 2017. Flow cytometry as a rapid analytical tool to determine physiological responses to changing O_2 and iron concentration by *Magnetospirillum gryphiswaldense* strain MSR-1. Sci. Rep. 7 (1), 11. https://doi.org/10.1038/s41598-017-13414-z.
Fernández-Castané, A., Li, H., Thomas, O.R.T., Overton, T.W., 2018. Development of a simple intensified fermentation strategy for growth of *Magnetospirillum gryphiswaldense* MSR-1: physiological responses to changing environmental conditions. N. Biotechnol. 46, 22–30. https://doi.org/10.1016/j.nbt.2018.05.1201.
Fernández-Castané, A., Li, H., Joseph, S., Ebeler, M., Franzreb, M., Bracewell, D.G., Overton, T.W., Thomas, O.R.T., 2021. Nanoparticle tracking analysis as a process analytical tool for characterising magnetosome preparations. Food Bioprod. Process. 127, 426–434. https://doi.org/10.1016/j.fbp.2021.03.013.
Fischer, A., Schmitz, M., Aichmayer, B., Fratzl, P., Faivre, D., 2011. Structural purity of magnetite nanoparticles in magnetotactic bacteria. J. R. Soc. Interface 8, 1011–1018. https://doi.org/10.1098/rsif.2010.0576.
Fischer, H., Mastrogiacomo, G., Löffler, J.F., Warthmann, R.J., Weidler, P.G., Gehring, A. U., 2008. Ferromagnetic resonance and magnetic characteristics of intact magnetosome chains in *Magnetospirillum gryphiswaldense*. Earth Planet. Sci. Lett. 270 (3-4), 200–208. https://doi.org/10.1016/j.epsl.2008.03.022.
Fischer, I., Franzreb, M., 2011. Direct determination of the composition of aqueous micellar two-phase systems (AMTPS) using potentiometric titration-A rapid tool for detergent-based bioseparation. Colloids Surf. 377, 97–102. https://doi.org/10.1016/j.colsurfa.2010.12.030.
Fischer, I., Franzreb, M., 2012. Nanoparticle mediated protein separation in aqueous micellar two-phase systems. Solv. Extr. Ion.-. Exch. 30 (1), 1–16. https://doi.org/10.1080/07366299.2011.581093.
Fischer, I., Hsu, C.-C., Gärtner, M., Müller, C., Overton, T.W., Thomas, O.R.T., Franzreb, M., 2013. Continuous protein purification using functionalized magnetic nanoparticles in aqueous micellar two-phase systems. J. Chromatogr. A 1305, 7–16. https://doi.org/10.1016/j.chroma.2013.06.011.
Frankel, R.B., Blakemore, R.P., 1980. Navigational compass in magnetic bacteria. J. Mag. Mag. Mat. 15-18 (3), 1562–1564. https://doi.org/10.1016/0304-8853(80)90409-6.
Franzreb, M., Reichert, C. (2006) Hochgradienten-Magnetabscheider, DE Patent 102004034541.
Galaev, I.Y., Mattiasson, B., 1993. Thermoreactive water-soluble polymers, nonionic surfactants, and hydrogels as reagents in biotechnology. Enz. Microb. Technol. 15 (5), 354–366. https://doi.org/10.1016/0141-0229(93)90122-I.
Gehring, A.U., Charilaou, M., García-Rubio, I., 2012. Oxidized magnetosomes in magnetotactic bacteria. J. Magn. Magn. Mater. 324, 1281–1284. https://doi.org/10.3390/microorganisms9091854.
Ginet, N., Pardoux, R., Adryanczyk, G., Garcia, D., Brutesco, C., Pignol, D., 2011. Single-step production of a recyclable nanobiocatalyst for organophosphate pesticides biodegradation using functionalized bacterial magnetosomes. PLoS One 6, 4–10. https://doi.org/10.1371/journal.pone.0021442.
Gorby, Y.A., Beveridge, T.J., Blakemore, R.P., 1988. Characterization of the bacterial magnetosome membrane. J. Bacteriol. 170, 834–841. https://doi.org/10.1128/jb.170.2.834-841.1988.
Griebel, R., Smith, Z., Merrick, J.M., 1968. Metabolism of poly-beta-hydroxybutyrate. I. Purification, composition, and properties of native poly-beta-hydroxybutyrate granules from *Bacillus megaterium*. Biochemistry 7, 3676–3681. https://doi.org/10.1021/bi00850a047.
Grünberg, K., Wawer, C., Tebo, B.M., Schuler, D., 2001. A large gene cluster encoding several magnetosome proteins is conserved in different species of magnetotactic bacteria. Appl. Environ. Microbiol. 67, 4573–4582. https://doi.org/10.1128/AEM.67.10.4573-4582.2001.
Grünberg, K., Müller, E.C., Otto, A., Reszka, R., Linder, D., Kube, M., Reinhardt, R., Schüler, D., 2004. Biochemical and proteomic analysis of the magnetosome membrane in *Magnetospirillum gryphiswaldense*. Appl. Environ. Microbiol. 70, 1040–1050. https://doi.org/10.1128/AEM.70.2.1040-1050.2004.
Gul, S., Khan, S.B., Rehman, I.U., Khan, M.A., Khan, M.I., 2019. A comprehensive review of magnetic nanomaterials modern day theranostics. Front. Mater. 6, 179 https://doi.org/10.3389/fmats.2019.00179.
Guo, F., Liu, Y., Chen, Y., Tang, T., Jiang, W., Li, Y., Li, J., 2011. A novel rapid and continuous procedure for large-scale purification of magnetosomes from *Magnetospirillum gryphiswaldense*. Appl. Microbiol. Biotechnol. 90, 1277–1283. https://doi.org/10.1007/s00253-011-3189-3.
Hafsi, M., Prévéral, S., Hoog, C., Hérault, J., Perrier, G.A., Lefèvre, C.T., Michel, C.T., Pignol, D., Doyen, J., Pourcher, T., Humbert, O., 2020. RGD-functionalized magnetosomes from *Magnetospirillum gryphiswaldense*. Appl. Microbiol. Biotechnol. 90, 1277–1283. https://doi.org/10.1016/j.nano.2019.102084.
Hamdous, Y., Chebbi, I., Mandawala, C., Le Fèvre, R., Guyot, F., Seksek, O., Alphandéry, E., 2017. Biocompatible coated magnetosome minerals with various organization and cellular interaction properties induce cytotoxicity towards RG-2 and GL-261 glioma cells in the presence of an alternating magnetic field. J. Nanobiotechnol. 15 (1), 74 https://doi.org/10.1186/s12951-017-0293-2.
Heyen, U., Schüler, D., 2003. Growth and magnetosome formation by microaerophilic *Magnetospirillum* strains in an oxygen-controlled fermentor. Appl. Microbiol. Biotechnol. 61, 536–544. https://doi.org/10.1007/s00253-002-1219-x.
Jacob, J.J., Suthindhiran, K., 2016. Magnetotactic bacteria and magnetosomes – Scope and challenges. Mater. Sci. Eng. C. 68, 919–928. https://doi.org/10.1016/j.msec.2016.07.049.
Katzmann, E., Müller, F.D., Lang, C., Messerer, M., Winklhofer, M., Pliztko, J.M., Schüler, D., 2011. Magnetosome chains are recruited to cellular division sites and split by asymmetric septation. Molecul. Microbiol. 82 (6), 1316–1329. ⟨https://doin.org/10.1111/j.1365-2958.2011.07874.x⟩.
Katzmann, E., Eibauer, M., Lin, W., Pan, Y., Plitzko, J.M., Schüler, D., 2013. Analysis of magnetosome chains in magnetotactic bacteria by magnetic measurements and automated image analysis of electron micrographs. Appl. Environ. Microbiol. 79, 7755–7762. https://doi.org/10.1128/AEM.02143-13.
Kobayashi, A., Kirschvink, J.L., Nash, C.Z., Kopp, R.E., Sauer, D.A., Bertani, L.E., Voorhout, W.F., Taguchi, T., 2006. Experimental observation of magnetosome chain collapse in magnetotactic bacteria: sedimentological, paleomagnetic, and evolutionary implications. Earth Planet. Sci. Lett. 245, 538–550. https://doi.org/10.1016/j.epsl.2006.03.041.
Krolitzki, E., Steck, S., Nazifi, A., Abt, M., Schwaminger, S.P., Berensmeier, S., 2023. How to design a low-cost pilot scale magnetic bioseparation process for protein separation from complex mixtures using in-line process analytics. Sep. Purif. Technol. 323, 24429. https://doi.org/10.1016/j.seppur.2023.124429.
Kuger, L., Arlt, C.R., Franzreb, M., 2022. Magnetic/flow controlled continuous size fractionation of magnetic nanoparticles using simulated moving bed chromatography. Talanta 240, 123160. https://doi.org/10.1016/j.talanta.2021.123160.
Kumari, M., Hirt, A.M., Uebe, R., Schüler, D., Tompa, É., Pósfai, M., Lorenz, W., Ahrentorp, F., Jonasson, C., Johansson, C., 2015. Experimental mixtures of superparamagnetic and single-domain magnetite with respect to Day-Dunlop plots. Geochem. Geophys. Geosyst. 16 (6), 1739–1752. https://doi.org/10.1002/2015GC005744.
Lang, C., Schüler, D., 2008. Expression of green fluorescent protein fused to magnetosome proteins in microaerophilic magnetotactic bacteria. Appl. Environ. Microbiol. 74, 4944–4953. https://doi.org/10.1128/AEM.00231-08.
Lee, N., Kim, H., Choi, S.H., Park, M., Kim, D., Kim, H.C., Choi, Y., Lin, S., Kim, B.H., Jung, H.S., Kim, H., 2011. Magnetosome-like ferrimagnetic iron oxide nanocubes for highly sensitive MRI of single cells and transplanted pancreatic islets. Proc. Natl. Acad. Sci. U. S. A. 108 (7), 2662–2667. https://doi.org/10.1073/pnas.1016409108.
Li, J., Pan, Y., Liu, Q., Qin, H., Deng, C., Che, R., Yang, X., 2010. A comparative study of magnetic properties between whole cells and isolated magnetosomes of *Magnetospirillum magneticum* AMB-1. Chin. Sci. Bull. 55 (1), 38–44. https://doi.org/10.1007/s11434-009-0333-x.
Liu, Y., Li, G.R., Guo, F.F., Jiang, W., Li, Y., Li, L.J., 2010. Large-scale production of magnetosomes by chemostat culture of *Magnetospirillum gryphiswaldense* at high cell density. Microb. Cell Factor. 9 (1), 1–8. https://doi.org/10.1186/1475-2859-9-99.
Lovitt, R.W., Jones, M., Collins, S.E., Coss, G.M., Yau, C.P., Attouch, C., 2000. Disruption of bakers' yeast using a disrupter of simple and novel geometry. Process Biochem. 36 (5), 415–421. https://doi.org/10.1186/1475-2859-9-99.
Meriño, S., Glanzman, S., 2016. Continuous flow centrifugation: importance in vector scale up. Cell Gene Ther. Insights 2 (5), 577–582. https://doi.org/10.18609/cgti.2016.069.
Majidi, S., Zeinali Sehrig, F., Farkhani, S.M., Soleymani Goloujeh, M., Akbarzadeh, A., 2016. Current methods for synthesis of magnetic nanoparticles. Artif. Cells, Nanomed., Biotechnol., Artif. Cells Nanomed. Biotechnol. 44 (2), 722–734. https://doi.org/10.3109/21691401.2014.982802.
Mickoleit, F., Borkner, C.B., Toro-Nahuelpan, M., Herold, H.M., Maier, D.S., Plitzko, J. M., Scheibel, T., Schüler, D., 2018. *In vivo* coating of bacterial magnetic nanoparticles by magnetosome expression of spider silk-inspired peptides. Biomacromolecules 19 (3), 962–972. https://doi.org/10.1021/acs.biomac.7b01749.
Mickoleit, F., Jörke, C., Richter, R., Rosenfeldt, S., Markert, S., Rehberg, I., Schenk, A.S., Bäumchen, O., Schüler, D., Clement, J.H., 2023. Long-term stability, biocompatibility, and magnetization of suspensions of isolated bacterial magnetosomes. Small, 2206244. https://doi.org/10.1002/smll.202206244.
Middelberg, A.P.J., 1995. Process-scale disruption of microorganisms. Biotech. Adv. 13, 491–551. https://doi.org/10.1016/0734-9750(95)02007-P.
Morita, M., Aizawa, M., Toi, H., Fukuhara, E., Hashimoto, K., 2011. Continuous flow ultracentrifuge system for production of infection prevention vaccines. Hitachi Rev. 60, 257–261.
Moskowitz, B.M., Frankel, R.B., Flanders, P.J., Blakemore, R.P., Schwartz, B.B., 1988. Magnetic properties of magnetotactic bacteria. J. Magn. Magn. Mater. 73 (3), 273–288. https://doi.org/10.1016/0304-8853(88)90093-5.
Oelmeier, S.A., Dismer, F., Hubbuch, J., 2011. Application of an aqueous two-phase systems high-throughput screening method to evaluate mAb HCP separation. Biotechnol. Bioeng. 108 (1), 69–81. https://doi.org/10.1002/bit.22900.
Orue, I., Marcano, L., Bender, P., García-Prieto, A., Valencia, S., Mawass, M.A., Gil-Cartón, D., Alba Venero, D., Honecker, D., García-Arribas, A., Fernández Barquin, L.,

Muela, A., Fdez-Gubieda, M.L., 2018. Configuration of the magnetosome chain: a natural magnetic nanoarchitecture. Nanoscale 10, 7407. https://doi.org/10.1039/c7nr08493e.

Peigneux, A., Valverde-Tercedor, C., Lopez-Moreno, R., Pérez-Gonzaléz, T., Fernández-Vivas, M.A., Jiménez-López, C., 2016. Learning from magnetotactic bacteria: a review on the synthesis of biomimetic nanoparticles mediated by magnetosome-associated proteins. J. Struct. Biol. 196, 75–84. https://doi.org/10.1016/j.jsb.2016.06.026.

Plan Sangnier, A., Preveral, S., Curcio, A., Silva, A.K., Lefèvre, C.T., Pignol, D., Lalatonne, Y., Wilhelm, C., 2018. Targeted thermal therapy with genetically engineered magnetite magnetosomes@ RGD: photothermia is far more efficient than magnetic hyperthermia. J. Control. Release 279, 271–281. https://doi.org/10.1016/j.jconrel.2018.04.036.

Rawlings, A.E., Somner, L.A., Fitzpatrick-Milton, M., Roebuck, T.P., Gwyn, C., Liravi, P., Seville, V., Neal, T.J., Mykhaylyk, O.O., Baldwin, S.A., Staniland, S.S., 2019. Artificial coiled coil biomineralisation protein for the synthesis of magnetic nanoparticles. Nat. Comm. 10 (1), 2873 https://doi.org/10.1038/s41467-019-10578-2.

Rosenfeldt, S., Mickoleit, F., Jörke, C., Clement, J.H., Markert, S., Jérôme, V., Schwarzinger, S., Freitag, R., Schüler, D., Uebe, R., Schenk, A.S., 2021. Towards standardized purification of bacterial magnetic nanoparticles for future in vivo applications. Acta Biomater. 120, 293–303. https://doi.org/10.1016/j.actbio2020.07.042.

Ruiz-Ruiz, F., López-Guajardo, E., Vázquez-Villegas, P., del Angel-Chong, M.E., Nigam, K.D.P., Willson, R.C., Rito-Palomares, M., 2019. Continuous aqueous two-phase extraction of microalgal C-phycocyanin using a coiled flow inverter. Chem. Eng. Process.: Process. Intensif. 142, 107554 https://doi.org/10.1016/j.cep.2019.107554.

Scheffel, A., Gruska, M., Faivre, D., Linaroudis, A., Plitzko, J.M., Schüler, D., 2006. An acidic protein aligns magnetosomes along a filamentous structure in magnetotactic bacteria. Nature 440, 110–114. https://doi.org/10.1038/nature04382.

Schüler, D., 2008. Genetics and cell biology of magnetosome formation in magnetotactic bacteria. FEMS Microbiol. Rev. 32, 654–672. https://doi.org/10.1111/j.1574-6976.2008.00116.x.

Schüler, D., Baeuerlein, E., 1998. Dynamics of iron uptake and Fe_3O_4 biomineralization during aerobic and microaerobic growth of *Magnetospirillum gryphiswaldense*. J. Bacteriol. 180 (1), 159–162. https://doi.org/10.1128/JB.180.1.159-162.1998.

Schüler, D., Frankel, R.B., 1999. Bacterial magnetosomes: microbiology, biomineralization and biotechnological applications. Appl. Microbiol. Biotechnol. 52, 464–473. https://doi.org/10.1007/s002530051547.

Schüler, D., Uhl, R., Bäuerlein, E., 1995. A simple light scattering method to assay magnetism in *Magnetospirillum gryphiswaldense*. FEMS Microbiol. Lett. 132 (1-2), 139–145. https://doi.org/10.1111/j.1574-6968.1995.tb07823.x.

Staniland, S.S., Moisescu, C., Benning, L.G., 2010. Cell division in magnetotactic bacteria splits magnetosome chain in half. J. Basic Microbiol. 50, 392–396. https://doi.org/10.1002/jobm.200900408.

Sun, J.B., Zhao, F., Tang, T., Jiang, W., Tian, J.S., Li, Y., Li, J.L., 2008. High-yield growth and magnetosome formation by *Magnetospirillum gryphiswaldense* MSR-1 in an oxygen-controlled fermentor supplied solely with air. Appl. Microbiol. Biotechnol. 79, 389–397. https://doi.org/10.1007/s00253-008-1453-y.

Sun, J., Li, Y., Liang, X.J., Wang, P.C., 2011. Bacterial magnetosome: a novel biogenetic magnetic targeted drug carrier with potential multifunctions. J. Nanomater. 2011, 469031 https://doi.org/10.1155/2011/469031.

Trakultamupatam, P., Scamehorn, J.F., Osuwan, S., 2004a. Scaling up cloud point extraction of aromatic contaminants from wastewater in a continuous rotating disk contactor. I. Effect of disk rotation speed and wastewater to surfactant ratio. Sep. Sci. Technol. 39 (3), 479–499. https://doi.org/10.1081/SS-120027991.

Trakultamupatam, P., Scamehorn, J.F., Osuwan, S., 2004b. Scaling up cloud point extraction of aromatic contaminants from wastewater in a continuous rotating disk contactor. II. Effect of operating temperature and added electrolyte. Sep. Sci. Technol. 39 (3), 501–516. https://doi.org/10.1081/SS-120027992.

Uebe, R., Junge, K., Henn, V., Poxleitner, G., Katzmann, E., Plitzko, J.M., Zarivach, R., Kasama, T., Wanner, G., Pósfai, M., Böttger, L., 2011. The cation diffusion facilitator proteins MamB and MamM of *Magnetospirillum gryphiswaldense* have distinct and complex functions and are involved in magnetite biomineralization and magnetosome membrane assembly. Molecul. Microbiol. 82 (4), 818–835. https://doi.org/10.1111/j.1365-2958.2011.07863.x.

Vargas, G., Cypriano, J., Correa, T., Leão, P., Bazylinski, D.A., Abreu, F., 2018. Applications of magnetotactic bacteria, magnetosomes and magnetosome crystals in biotechnology and nanotechnology: mini-review. Molecules 23 (10), 2438. https://doi.org/10.3390/molecules23102438.

Van Hee, P., Middelberg, A.P., Van Der Lans, R.G., Van Der Wielen, L.A., 2004. Relation between cell disruption conditions, cell debris particle size, and inclusion body release. Biotechnol. Bioeng. 88 (1), 100–110. https://doi.org/10.1002/bit.20343.

Van Hee, P., Elumbaring, A.C., van der Lans, R.G., Van der Wielen, L.A., 2006. Selective recovery of polyhydroxyalkanoate inclusion bodies from fermentation broth by dissolved-air flotation. J. Colloid Interface Sci. 297 (2), 595–606. https://doi.org/10.1016/j.jcis.2005.11.019.

Wacker, R., Ceyhan, B., Alhorn, P., Schüler, D., Lang, C., Niemeyer, C.M., 2007. Magneto immuno-PCR: a novel immunoassay based on biogenic magnetosome nanoparticles. Biochem. Biophys. Res. Commun. 357 (2), 391–396. https://doi.org/10.1016/j.bbrc.2007.03.156.

Wang, X., Wang, Q., Zhang, Y., Wang, Y., Zhou, Y., Zhang, W., Wen, T., Li, L., Zuo, M., Zhang, Z., Tian, J., 2016. Transcriptome analysis reveals physiological characteristics required for magnetosome formation in *Magnetospirillum gryphiswaldense* MSR-1. Environ. Microbiol. Rep. 8 (3), 371–381. https://doi.org/10.1111/1758-2229.12395.

Wang, X., Wang, J.G., Geng, Y.Y., Wang, J.J., Zhang, X.M., Yang, S.S., Jiang, W., Liu, W. Q., 2018. An enhanced anti-tumor effect of apoptin-cecropin B on human hepatoma cells by using bacterial magnetic particle gene delivery system. Biochem. Biophys. Res. Commun. 496 (2), 719–725. https://doi.org/10.1016/j.bbrc.2018.01.108.

Widdel, F., Bak, F., 1992. Gram-negative mesophilic sulfate-reducing bacteria. In: Balows, A., Troper, H., Dworkin, M., Harder, W., Schleifer, K. (Eds.), The Prokaryotes. Springer Berlin Heidelberg, New York, pp. 3352–3378. https://doi.org/10.1007/978-1-4757-2191-1_21.

Xiang, L., Wei, J., Jianbo, S., Guili, W., Feng, G., Ying, L., 2007. Purified and sterilized magnetosomes from *Magnetospirillum gryphiswaldense* MSR-1 were not toxic to mouse fibroblasts in vitro. Lett. Appl. Microbiol. 45, 75–81. https://doi.org/10.1111/j.1472-765X.2007.02143.x.

Yang, J., Li, S., Huang, X., Tang, T., Jiang, W., Zhang, T., Li, Y., 2013. A key time point for cell growth and magnetosome synthesis of *Magnetospirillum gryphiswaldense* based on real-time analysis of physiological factors. Front. Microbiol. 4, 1–7. https://doi.org/10.3389/fmicb.2013.00210.

Zhang, T., Pan, Y., 2018. Constraining the magnetic properties of ultrafine- and fine-grained biogenic magnetite. Earth Planets Space 70, 206. https://doi.org/10.1186/s40623-018-0978-2.

Zhang, Y., Zhang, X., Jiang, W., Li, Y., Li, J., 2011. Semicontinuous culture of *Magnetospirillum gryphiswaldense* MSR-1 cells in an autofermentor by nutrient-balanced and isosmotic feeding strategies. Appl. Environ. Microbiol. 77, 5851–5856. https://doi.org/10.1128/AEM.05962-11.

Zheng, H., Schenk, J., Spreitzer, D., Wolfinger, T., Daghagheleh, O., 2021. Review on the oxidation behaviors and kinetics of magnetite in particle scale. Steel Res. Int. 92 (8), 2000687 https://doi.org/10.1002/srin.202000687.